



**An Investigation of the Opacity of High-Z  
Mixtures**

**Ping Wang and J.J. MacFarlane**

**May 1996**

**UWFDM-1013**

***FUSION TECHNOLOGY INSTITUTE  
UNIVERSITY OF WISCONSIN  
MADISON WISCONSIN***

### **DISCLAIMER**

This report was prepared as an account of work sponsored by an agency of the United States Government. Neither the United States Government, nor any agency thereof, nor any of their employees, makes any warranty, express or implied, or assumes any legal liability or responsibility for the accuracy, completeness, or usefulness of any information, apparatus, product, or process disclosed, or represents that its use would not infringe privately owned rights. Reference herein to any specific commercial product, process, or service by trade name, trademark, manufacturer, or otherwise, does not necessarily constitute or imply its endorsement, recommendation, or favoring by the United States Government or any agency thereof. The views and opinions of authors expressed herein do not necessarily state or reflect those of the United States Government or any agency thereof.

# **An Investigation of the Opacity of High-Z Mixtures**

Ping Wang and J.J. MacFarlane

Fusion Technology Institute  
University of Wisconsin  
1500 Engineering Drive  
Madison, WI 53706

<http://fti.neep.wisc.edu>

May 1996

UWFDM-1013

# **An Investigation of the Opacity of High-Z Mixtures**

Ping Wang and Joseph J. MacFarlane

Fusion Technology Institute  
University of Wisconsin-Madison  
1500 Johnson Drive  
Madison, WI 53706

May 1996

UWFDM-1013

# Contents

<b>1. Introduction</b>	<b>1</b>
<b>2. Opacity Calculations for High-Z Materials</b>	<b>3</b>
2.1. Physical Models . . . . .	3
2.2. Opacity Calculations for Pure Gold, Samarium, and Gadolinium . . . . .	5
<b>3. The Opacity of High-Z Mixtures</b>	<b>27</b>
<b>4. Radiation Burnthrough Simulations for High-Z Mixtures</b>	<b>35</b>

## 1. Introduction

The purpose of this report is to provide a detailed description of work performed for Lawrence Livermore National Laboratory (LLNL) during the period December 1995 - May 1996. This work has been concentrated primarily in two areas. First, we have calculated and supplied Au opacity data tables to LLNL for use with the HYADES code to model thermal wave propagation in NOVA and NIF hohlraums. Second, we have investigated opacity characteristics of high-Z materials (Au, Sm, and Gd) and their mixtures (Au-Sm and Au-Gd). Using the calculated opacities, we have performed radiation-hydrodynamics simulations of radiation burnthrough experiments to investigate potential enhancements in the wall albedo of high-Z mixtures.

Table 1.1 shows the list of tasks for our contracted work with LLNL. Each of these tasks will be described in detail below. In Section II, the models we used for high-Z opacity calculations are described. Our calculations are compared with available experimental data to assess their reliability. In Section III, we study the opacity characteristics of pure gold, samarium, and gadolinium in the density range of  $0.01 \text{ g/cm}^3$  to  $20 \text{ g/cm}^3$  and temperature range of 10 eV to 300 eV which are relevant to NOVA and NIF hohlraum plasma conditions. Finally in Section IV, we present results from 1-D radiation-hydrodynamics simulations of Au and Au-Gd mixture radiation burnthrough experiments.

**Table 1.1. Tasks for December 1995 to May 1996**

---

1. Calculate Au opacity in the density range of  $0.001 \text{ g/cm}^3$  to about  $500 \text{ g/cm}^3$  and temperatures in the range of 10 eV to 300 eV using the EOSOPA code developed at the University of Wisconsin. This data should be provided in tabular form for use with the HYADES code to model thermal wave propagation in NOVA and NIF hohlraums.
  2. Using the codes available at the University of Wisconsin (i.e. EOSOPA and BUCKY), investigate mixtures of materials that could be used for hohlraum walls and that have the following properties:
    - a. The Rosseland mean opacity of the mixture must be sufficiently higher than that of Au in the density and temperature ranges of interest (see Item 1) such that the albedo of the material is 5 to 10% higher than that of pure Au.
    - b. The mixture must be chemically and mechanically stable. That is, a hohlraum fabricated from this material must not degrade over time and the hohlraum itself must be sufficiently sturdy to support diagnostic packages and shields as well as support the weight of the assembly on the target stalk, just as the conventional, pure Au hohlraums are presently capable.
  3. Interact with the target fabrication group at LLNL to ensure that the new material can, in fact, be used for hohlraum fabrication. Also, can “alternate” fabrication techniques be used in making the hohlraums? For example, can a hohlraum fabricated with alternating layers of different elements work just as well as a hohlraum whose walls contain the same elements and fractional composition uniformly mixed together.
-

## 2. Opacity Calculations for High-Z Materials

### 2.1. Physical Models

The calculation of opacities for high- $Z$ , as well as low- $Z$ , plasmas requires models for computing atomic structure, level populations, radiative transition cross sections, spectral line shapes, and plasma effects. However, the atomic structure of high- $Z$  atomic systems is much more complicated due to many electronic configurations with open  $d$  and  $f$  shells. Due to angular momentum coupling, configurations of this kind can have hundreds, or even thousands, of levels. For example,  $4f^7 5d^2 6p^1$ , a low excited configuration of neutral Gd, contains 24662 LS terms and 78822 fine-structure levels. The possible transitions between these levels are so numerous that it is impractical to use a detailed term accounting (DTA) model, which is a standard approach used for low- $Z$  atomic systems, to calculate high- $Z$  opacities. However, the term splitting in a high- $Z$  atomic system significantly affects the opacities and therefore must be appropriately accounted for in modeling high- $Z$  atomic systems. It has been found [1] that even for intermediate- $Z$  systems such as iron, the neglect of term splitting in opacity calculations can result in errors as large as a factor of 10. In our calculations, we use a detailed configuration accounting (DCA) method, but with term splitting effects included using an unresolved transition array (UTA) model assuming  $j - j$  coupling [2]. The UTA model treats the superposition of many overlapping, intrinsically broadened bound-bound transitions resulting from two electronic configurations as a single spectral feature. Each configuration-configuration transition array is then characterized by average quantities such as total intensity, average transition energy, and variance, which is used to account for term splitting effects in a statistical manner. For high- $Z$  atomic systems, we calculate these average quantities using Dirac-Fock-Slater [3,4] self-consistent field potentials. The ionization fractions and configuration populations are calculated assuming local thermodynamic equilibrium (LTE).

To illustrate the spectral characteristics of the UTA model, let us consider the transition array  $\text{Au}^{+44} 4p^4 4d^2 - 4p^4 4f^1$ . Figure 2.1 shows the detailed line structure computed for this transition array using a relativistic single configuration Hartree-Fock model with intermediate coupling. In this “stick” spectrum, each line has zero width and has a strength given by the oscillator strength times the statistical weight. By comparison, the UTA model treats this detailed line structure using a single configuration-to-configuration transition with an effective line profile shown by the curve in Fig. 2.1. The ability of the UTA model to treat complex transition arrays as a single transition — with a profile which approximates the opacity distribution of the array — greatly simplifies the calculation of

Au:  $4p^4 4d^1 - 4p^4 4f^1$

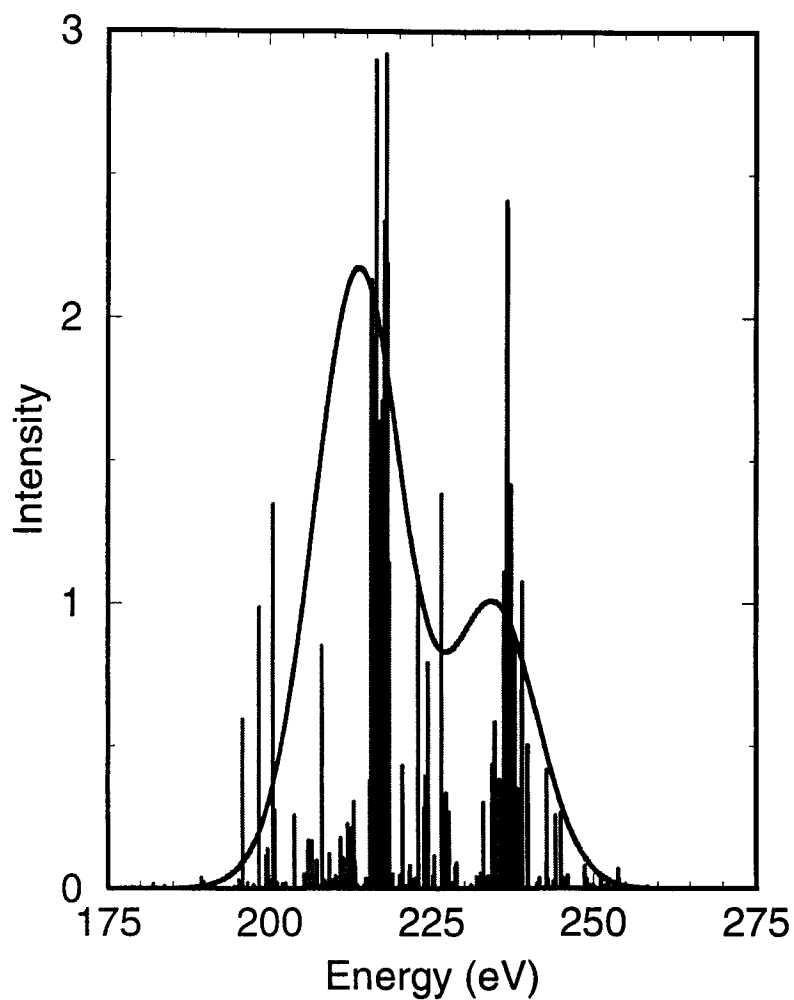


Figure 2.1. Calculated spectrum for  $\text{Au}^{44} 4p^4 4d^1 - 4p^4 4f^1$  transition. Each line is represented with a height proportional to its strength. The solid curve is the calculated UTA profile.

high-Z opacities. This allows a large number of configurations to be considered in opacity calculations.

To test the accuracy of our UTA opacity calculations we have compared our calculated absorption spectra for iron and germanium with experimental data [1,5]. Figure 2.2 shows our calculated absorption spectra for Fe at  $T = 59$  eV,  $\rho = 0.0127$  g/cm<sup>3</sup>, areal density of 272  $\mu\text{g}/\text{cm}^2$  (top), and Ge at  $T = 76$  eV,  $\rho = 0.05$  g/cm<sup>3</sup>, and areal density of 160  $\mu\text{g}/\text{cm}^2$ . These are the experimentally determined plasma conditions [1,5]. It can be seen that our UTA calculations are in good agreement with the observed spectra in both cases. The calculated Rosseland and Planck mean opacities for iron are  $\overline{\chi}_R = 4377$  cm<sup>2</sup>/g and  $\overline{\chi}_P = 8459$  cm<sup>2</sup>/g. These are also in good agreement with the experimental results, which are  $4400 \pm 600$  cm<sup>2</sup>/g and  $8200 \pm 700$  cm<sup>2</sup>/g, respectively.

Another benchmark we have done is to apply our UTA Au opacity data to simulations of Au radiation burnthrough experiments performed at NOVA [6]. The calculations were performed using BUCKY-1 [7], which is a 1-D Lagrangian radiation-hydrodynamics code. In these simulations, a multiangle radiation transport model was used with 100 frequency groups. A time-dependent radiation temperature boundary condition (with a Planckian spectrum) was applied to one side of the Au. The peak radiation temperature of 252 eV used in the simulation is consistent with the “wall temperature” measured by DANTE [6] and assuming an albedo of 0.8. Figure 2.3 shows a comparison of the calculated rear side fluxes for 1 and 2  $\mu\text{m}$ -thick foils (top) with experimental x-ray streak camera data (bottom). For both foil thicknesses, reasonably good agreement is found in the times at which the x-ray wave burns through the Au foils. These comparisons with experimental data for both the intermediate-Z transmission measurements and Au radiation burnthrough experiments give us the confidence that our UTA opacity calculation for high-Z plasmas should be reasonably accurate.

## 2.2. Opacity Calculations for Pure Gold, Samarium, and Gadolinium

Using our opacity code, EOSOPA, we have calculated opacities for gold, samarium, and gadolinium. The calculated absorption coefficient for a pure gold plasma at  $T=200$  eV and  $\rho = 0.1$  g/cm<sup>3</sup>, which is a typical NOVA hohlraum plasma condition, is shown in Fig. 2.4. For these conditions, the average charge state for the gold plasma is 34, with the dominant ions ranging from Nb-like to Ag-like. Also shown in Fig. 2.4 is the ratio of the *accumulated*

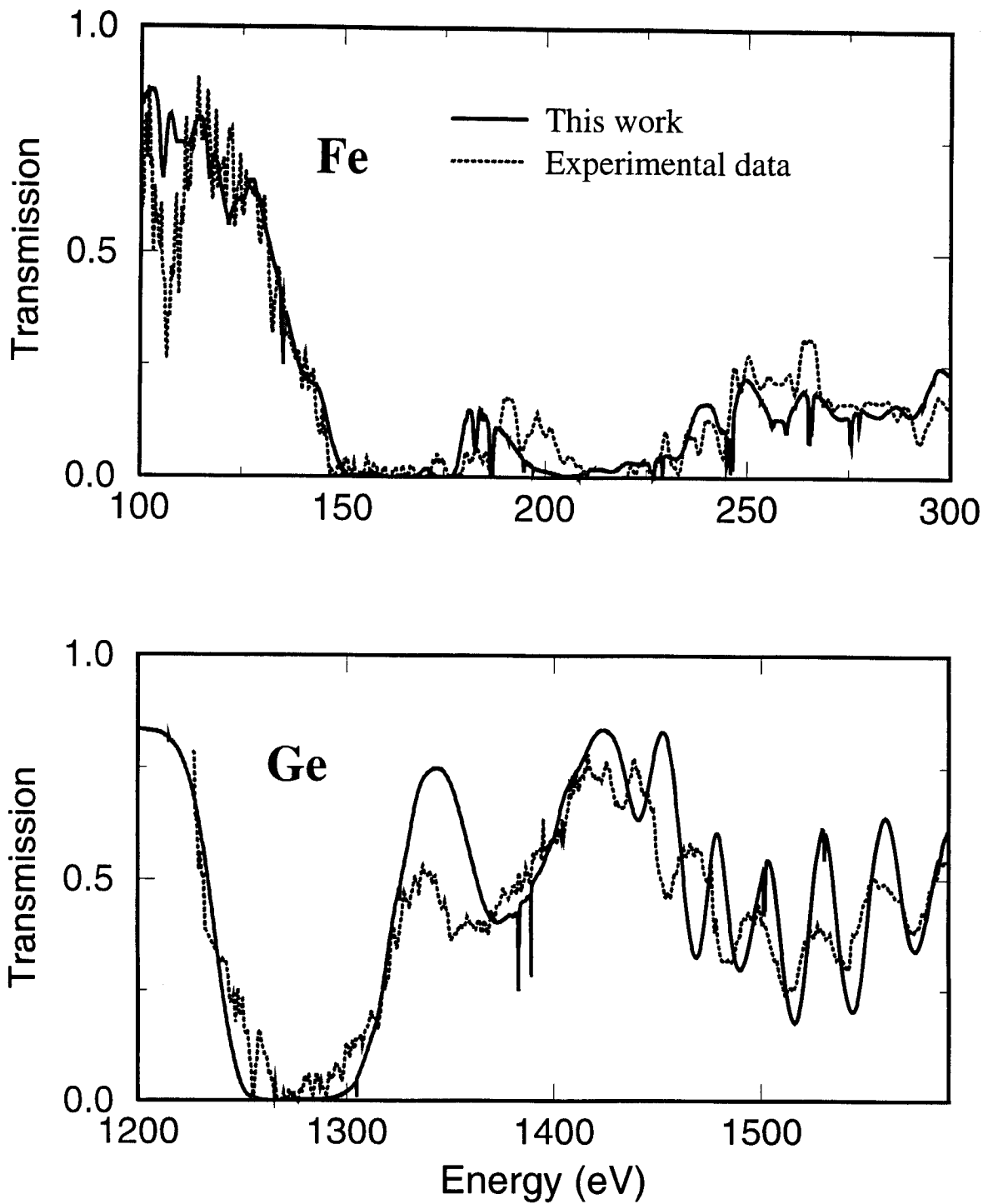


Figure 2.2. (Top) Comparison of experimental transmission data (dotted line) and calculations for an iron plasma of  $\rho = 1.27 \times 10^{-2} \text{ g/cm}^3$ ,  $T = 59 \text{ eV}$ , and areal density of  $272 \mu\text{g cm}^{-2}$ . (Bottom) Same for a germanium plasma of  $\rho = 0.05 \text{ g/cm}^3$ ,  $T = 76 \text{ eV}$ , and areal density of  $160 \mu\text{g cm}^{-2}$ .

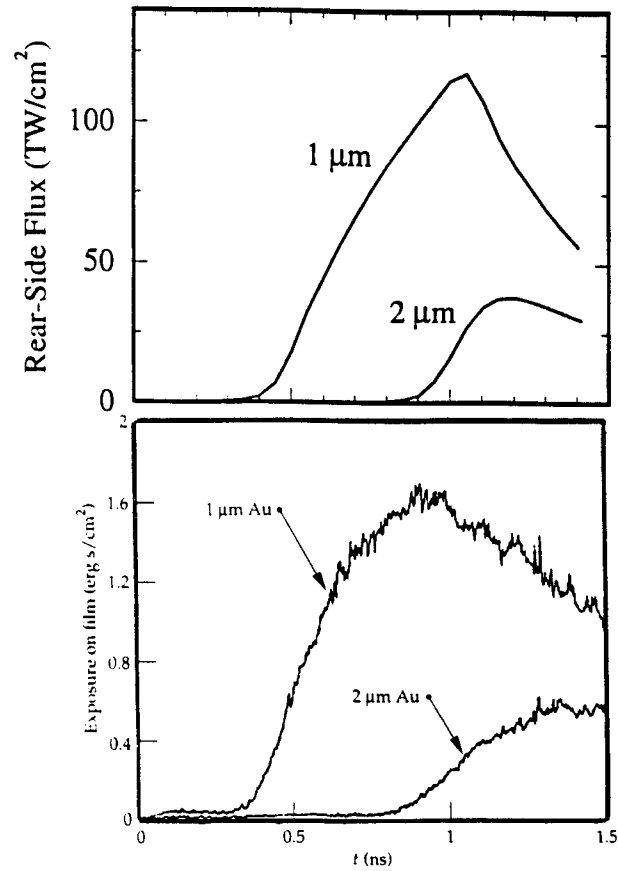


Figure 2.3. Comparison of the calculated rear side fluxes for 1 and 2  $\mu\text{m}$ -thick foils (top) with experimental x-ray streak camera data (bottom) of Au radiation burnthrough.

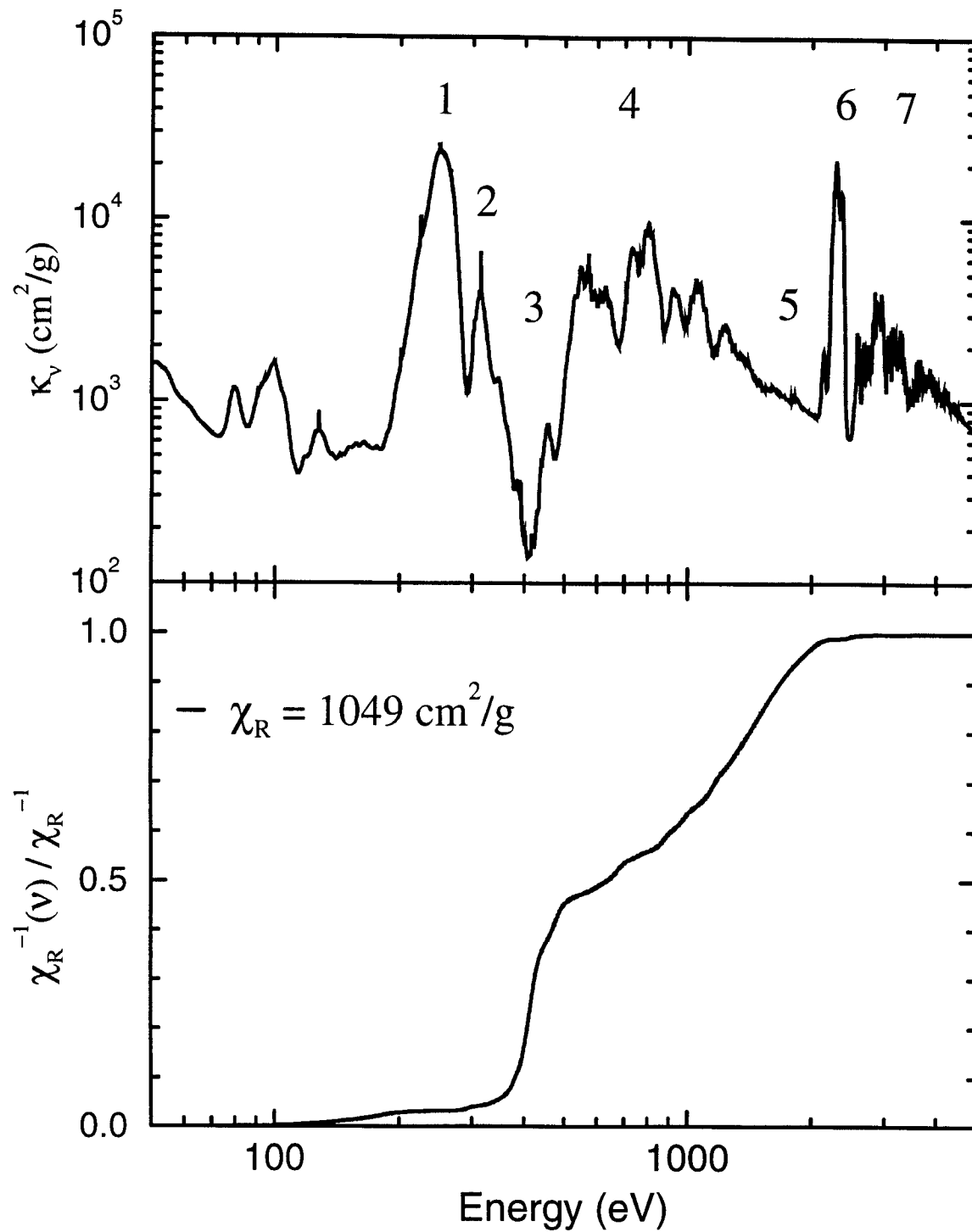


Figure 2.4. Calculated opacity for gold at  $T = 200$  eV,  $\rho = 0.1$  g/cm<sup>3</sup>. (Top) Absorption coefficient. (Bottom) Relative cumulative contribution to the Rosseland mean opacity as a function of frequency.

Rosseland mean, defined as:

$$\chi_R^{-1}(\nu) = \left( \frac{\pi}{4\sigma_R T^3} \right) \int_0^\nu \kappa_\nu^{-1} \left( \frac{dB_\nu}{dT} \right), \quad (1)$$

to the *total* Rosseland mean

$$\chi_{R,TOT}^{-1} = \left( \frac{\pi}{4\sigma_R T^3} \right) \int_0^\infty \kappa_\nu^{-1} \left( \frac{dB_\nu}{dT} \right), \quad (2)$$

where  $\sigma_R$  is Stefan-Boltzmann constant and  $B_\nu$  is the Planck function. Note that the integral is evaluated from 0 to  $\nu$  in Eq. (1), while it is evaluated from 0 to  $\infty$  in Eq. (2). The ratio provides an indication of the relative contribution of different frequency regions to the Rosseland mean opacity. Several features of interest are identified in Fig. 2.4: (1) (2) strong absorption features resulting from  $4d \rightarrow 4f$  and  $4p \rightarrow 4d$  transitions; (3) an absorption valley caused by the gap between the transitions of  $n = 4 \rightarrow n = 4$  and  $n = 4 \rightarrow n > 4$ ; (4) absorption features corresponding to the transitions  $n = 4 \rightarrow n > 4$ ; (5) an absorption valley between the N-band and M-band; (6) a strong absorption feature arising from  $3d \rightarrow 4f$  transitions; and (7) additional M-band absorption features ( $n = 3 \rightarrow n \geq 4$ ).

The bottom plot in Fig. 2.4 shows that only about 5% of the total Rosseland mean opacity comes from opacity at  $h\nu < 300$  eV. Similarly, there is little contribution above photon energies of 2 keV. For these conditions, roughly 45% of the Rosseland mean is due to the opacity “hole” at  $h\nu \approx 400$  eV (label 3). Also, it is seen that about 35% is due to the  $h\nu \approx 1 - 2$  keV region. Several calculated spectra for pure gold plasmas in different temperature and density conditions are shown in Figs. 2.5 through 2.7. It can be seen that over this range of plasma conditions, the two major absorption valleys (regions 3 and 5 of Fig. 2.4) are seen in all cases. Because the Rosseland mean opacity is a harmonic mean, it is most sensitive to regions of low absorption. The Rosseland mean opacities are therefore sensitive to the depth and width of these two major absorption valleys. Note that at the relatively low densities and high temperatures the hole near 400 – 600 eV widens. This occurs as the number of states with  $4f$  electrons decreases due to ionization. In Fig. 2.8 we compare the spectral region contributions to the Rosseland mean opacity in three different temperatures. We see that as the temperature increases, the absorption valley near  $h\nu = 400$  eV becomes deeper and wider and therefore contributes more to the Rosseland mean opacity. It is also seen that at lower temperatures ( $\lesssim 150$  eV), the hole near  $h\nu \approx 150$  eV begins to make a significant contribution to the Rosseland opacity.

In the temperature and density range of interest, these absorption valleys near 400 eV and 1 – 2 keV contribute significantly to the Rosseland mean opacity. By mixing

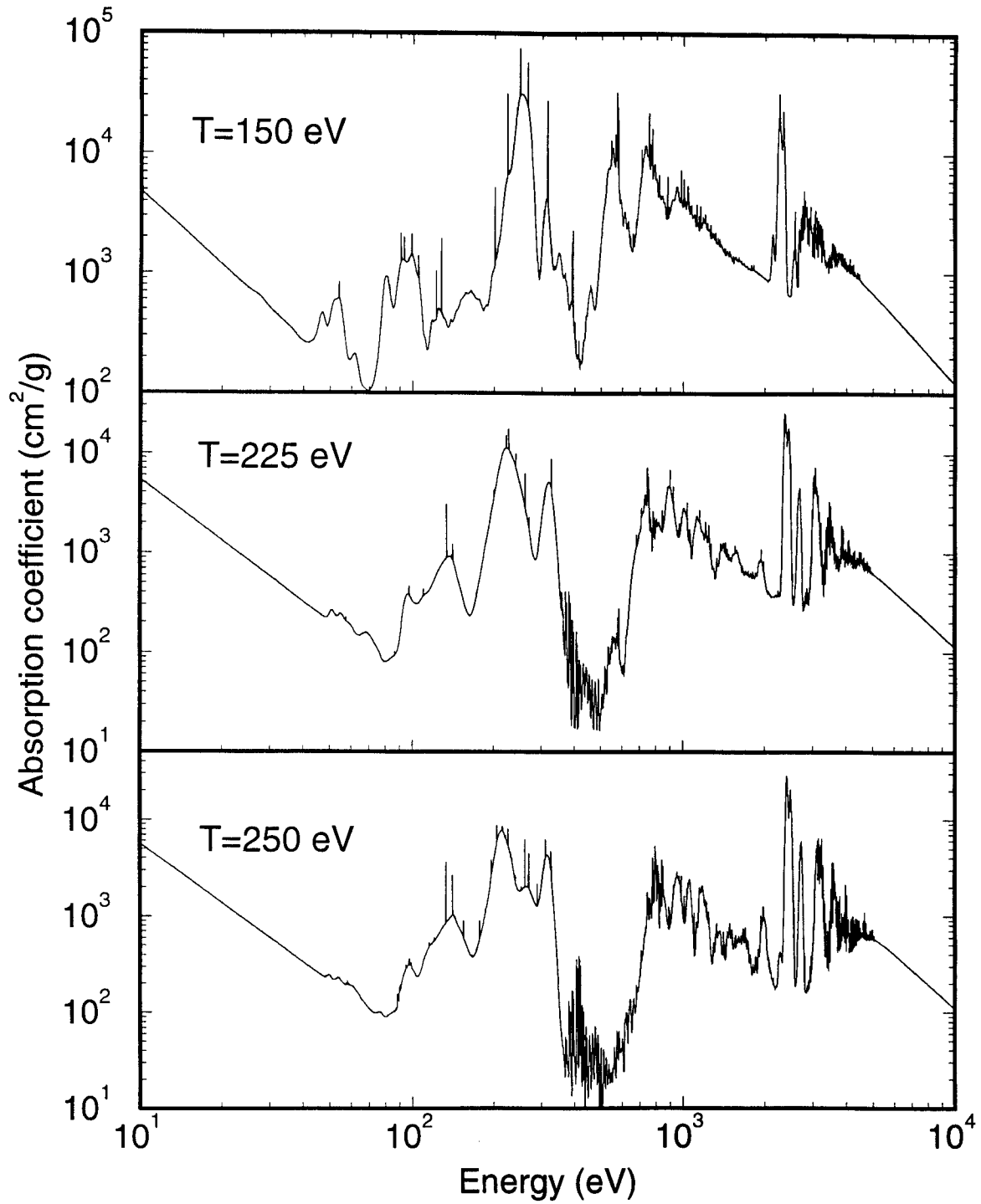


Figure 2.5. Calculated opacity for gold at  $\rho = 0.01$  g/cm<sup>3</sup> and three different temperatures. For  $T = 150$  eV,  $\bar{Z} = 32.4$  and  $\chi_R = 1474$  cm<sup>2</sup>/g; for  $T = 225$  eV,  $\bar{Z} = 42$  and  $\chi_R = 270$  cm<sup>2</sup>/g; for  $T = 250$  eV,  $\bar{Z} = 45$  and  $\chi_R = 170$  cm<sup>2</sup>/g.

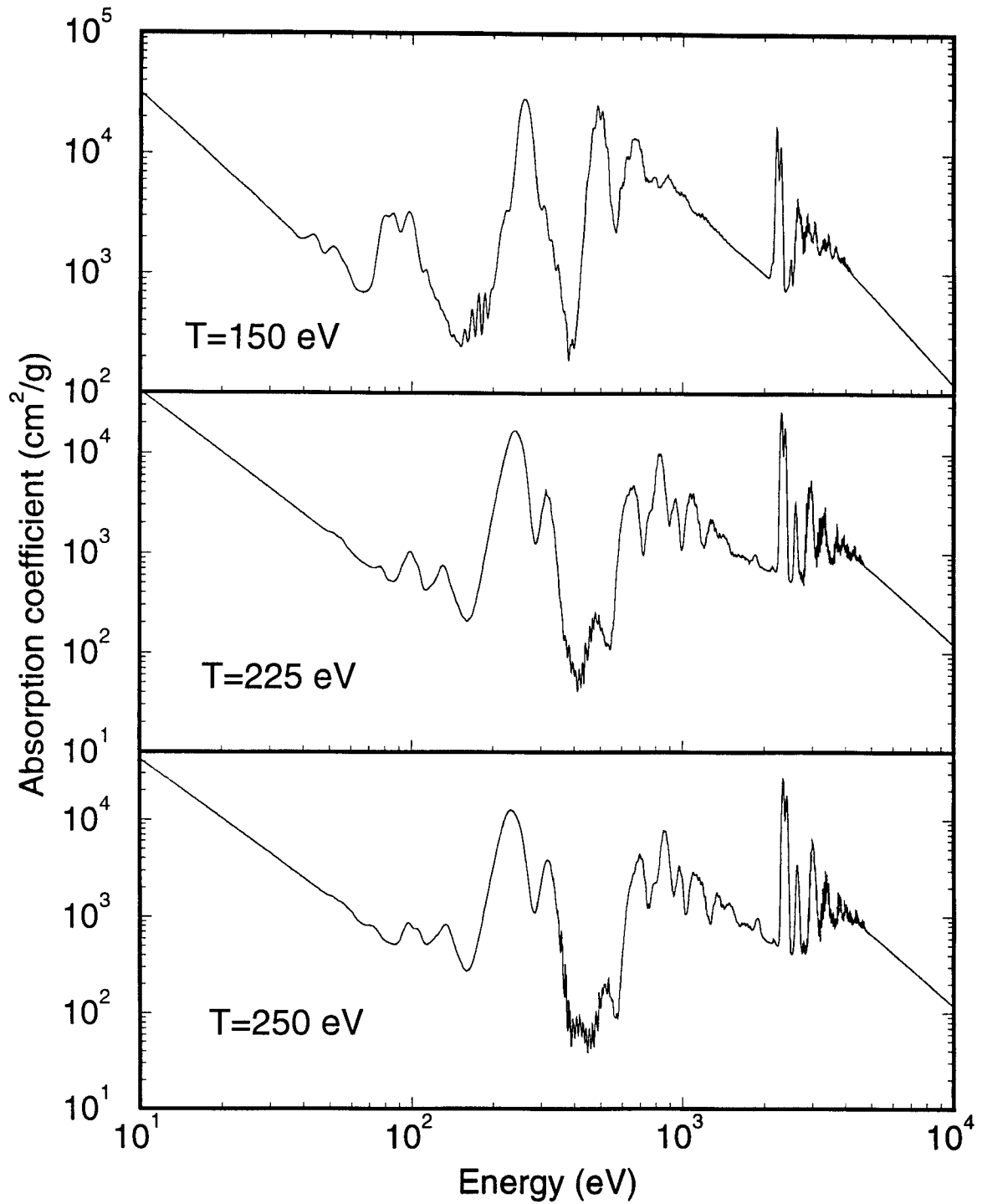


Figure 2.6. Calculated opacity for gold at  $\rho = 0.1$  g/cm<sup>3</sup> and three different temperatures. For  $T = 150$  eV,  $\bar{Z} = 28$  and  $\chi_R = 2200$  cm<sup>2</sup>/g; or  $T = 225$  eV,  $\bar{Z} = 37$  and  $\chi_R = 670$  cm<sup>2</sup>/g; for  $T = 250$  eV,  $\bar{Z} = 39$  and  $\chi_R = 570$  cm<sup>2</sup>/g.

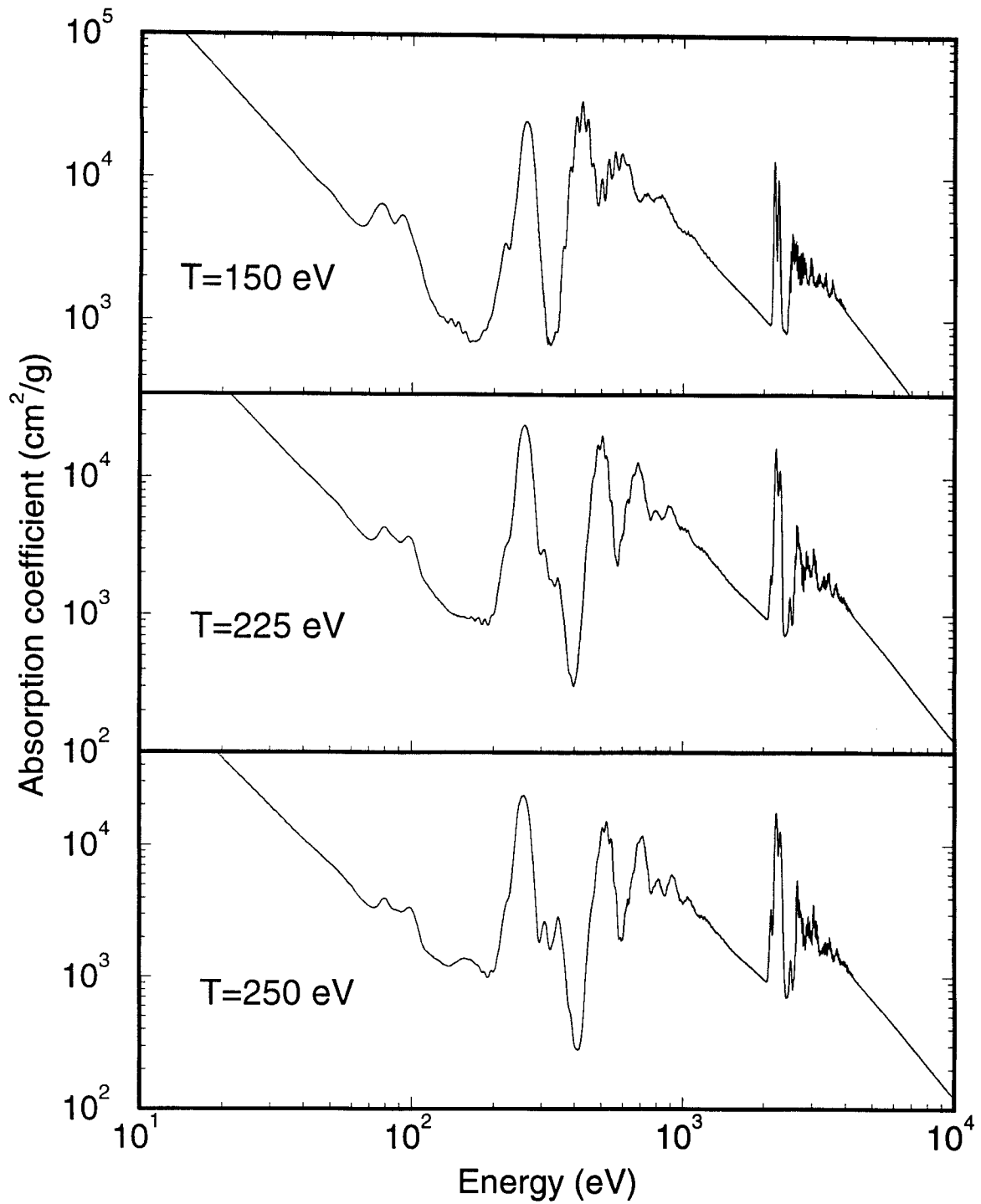


Figure 2.7. Calculated opacity for gold at  $\rho = 1.0 \text{ g/cm}^3$  and three different temperatures. For  $T = 150 \text{ eV}$ ,  $\bar{Z} = 24$  and  $\chi_R = 4120 \text{ cm}^2/\text{g}$ ; for  $T = 225 \text{ eV}$ ,  $\bar{Z} = 28$  and  $\chi_R = 2470 \text{ cm}^2/\text{g}$ ; for  $T = 250 \text{ eV}$ ,  $\bar{Z} = 30$  and  $\chi_R = 2190 \text{ cm}^2/\text{g}$ .

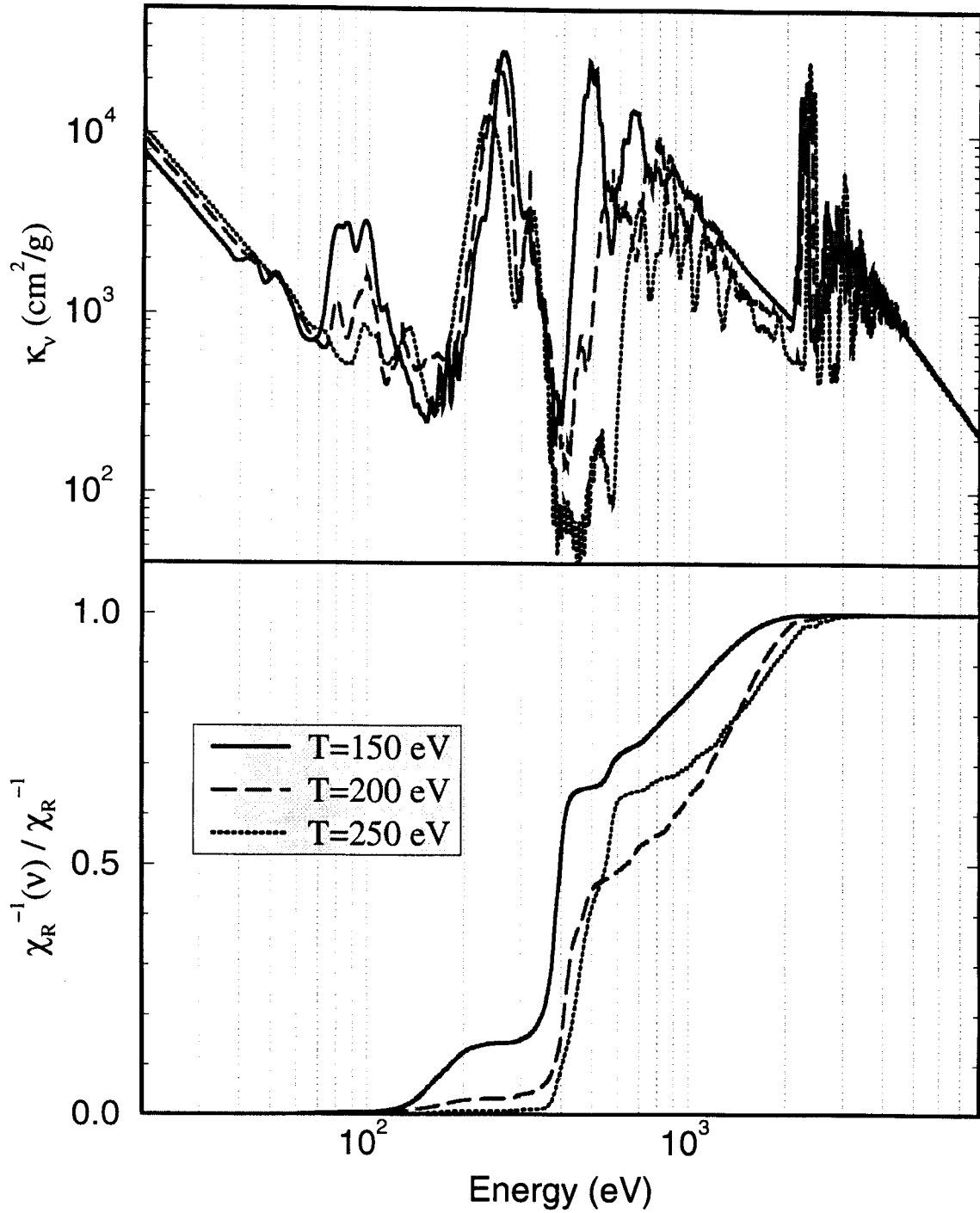


Figure 2.8. Calculated opacity for gold at  $\rho = 0.1 \text{ g/cm}^3$  and three different temperatures. (Top) Absorption coefficient. (Bottom) Relative cumulative contribution to the Rosseland mean opacity as a function of frequency.

gold with another high-Z element which has a high opacity in these regions, the Rosseland mean opacity can be increased. Thus, it is of value to identify another high-Z species to mix with Au whose opacities are relatively high at these photon energies.

Examination of the basic atomic structure data for the elements on the lanthanide series indicates that the transition energies of the major absorption peaks of these elements are about forty to fifty percent smaller than those of the corresponding transitions in gold. These major absorption peaks roughly lay in the regions where major absorption valleys of Au appear.

In Figs. 2.9 and 2.10 we show the absorption spectrum for Sm and Gd at  $T=200$  eV and  $\rho = 0.1$  g/cm<sup>3</sup>. Several major absorption features are identified as follows: (1),(2) are absorption features resulting from  $4s \rightarrow 4p$ ,  $4p \rightarrow 4d$ , and  $4d \rightarrow 4f$  transitions; (4),(5),(6) are absorption features resulting from  $n = 4 \rightarrow n > 4$  transitions; (7),(8),(9) are absorption features resulting from  $n = 3 \rightarrow n > 3$  transitions; and (10) are L-band absorption features. Note that for both elements the strong M- and N-band absorption features lay in the frequency regions where major absorption valleys of Au appear.

In Figs. 2.11 and 2.12 we show calculated absorption coefficients for Sm and Gd at several different temperatures. Also shown are the corresponding spectra of gold. It can be seen that in all cases the major absorption peaks of Sm and Gd ( $n = 3 \rightarrow n > 3$  and  $n = 4 \rightarrow n > 4$ ) nicely fill in the two major absorption valleys of gold. Because of this, an enhancement of the Rosseland mean opacity can be achieved by mixing Au with Sm or Gd.

Figures 2.13 to 2.15 show the Rosseland mean opacities of Au, Sm, and Gd at three different densities as a function of temperature. The overall trend is that the Rosseland mean opacity decreases as the temperature increases. However, an interesting feature in these plots is that the Rosseland mean opacity exhibits plateaus in several temperature regions. For example, the Rosseland mean opacity curve of Au at the density of 0.1 g/cm<sup>3</sup> exhibits plateaus near  $T = 185$  eV and  $T = 800$  eV. The Sm Rosseland mean opacity curves also exhibit a plateau near  $T = 300$  eV. This temperature dependence has to do with changes in the ionization distribution. To understand this, we investigate the N- and M-shell electron populations as a function of temperature, and compare them with the corresponding Rosseland mean opacities. The results are shown in Figs. 2.16 through 2.19. It can be seen that the formation of the plateaus in Rosseland mean opacities is closely related to the depopulation processes of the N- and M-shell electrons. For Au at 0.01 g/cm<sup>3</sup> (Fig. 2.17), the first plateau near  $T = 150$  eV is caused by the strong N-band absorption. This does not show a significant decrease until most of the  $4f$  electrons are depopulated.

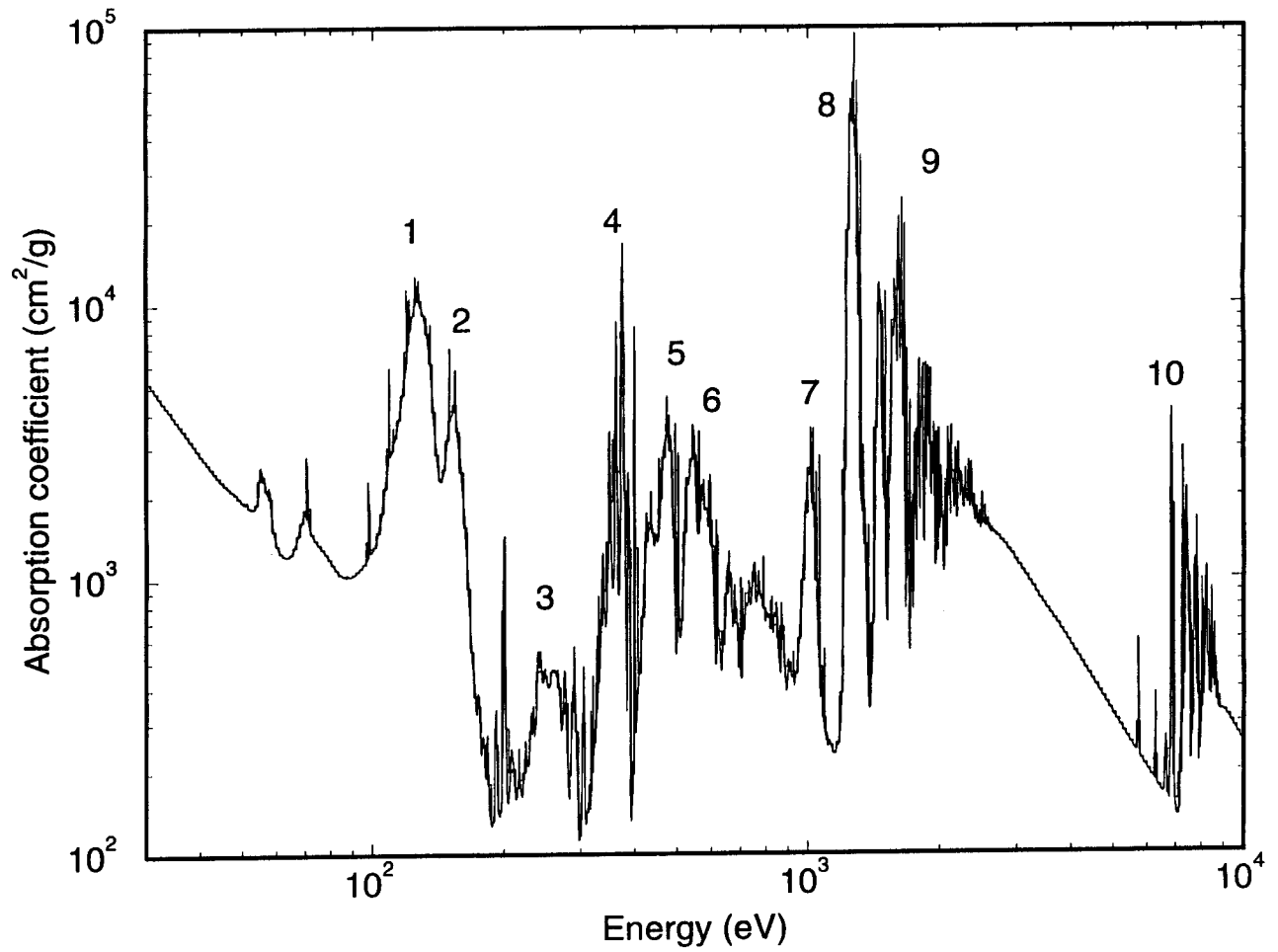


Figure 2.9. Calculated opacity for pure Sm at  $T = 200$  eV,  $\rho = 0.1$  g/cm<sup>3</sup>. Dominant absorption features are identified.

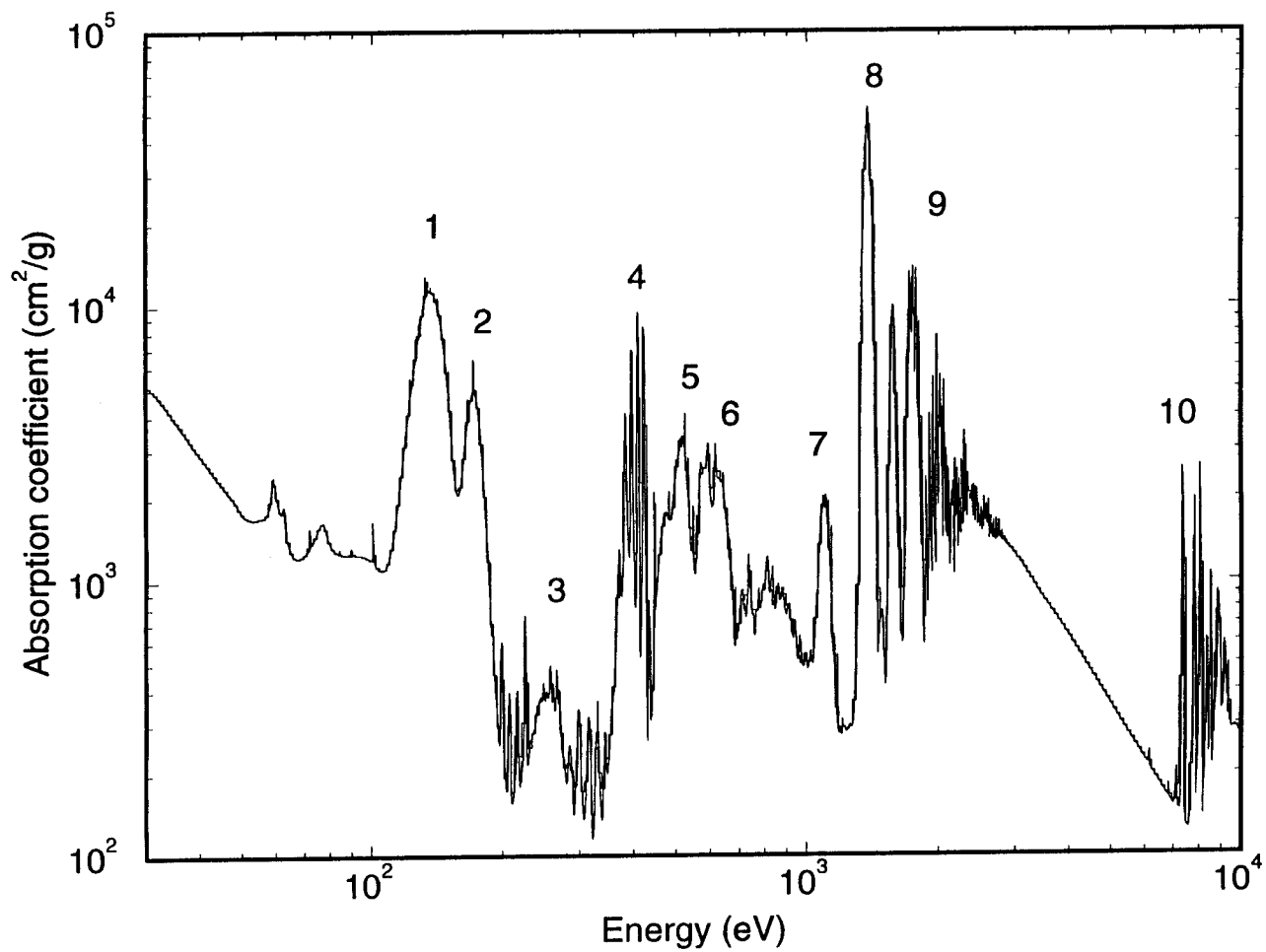


Figure 2.10. Calculated opacity for pure Gd at  $T = 200$  eV,  $\rho = 0.1$  g/cm<sup>3</sup>. Dominant absorption features are identified.

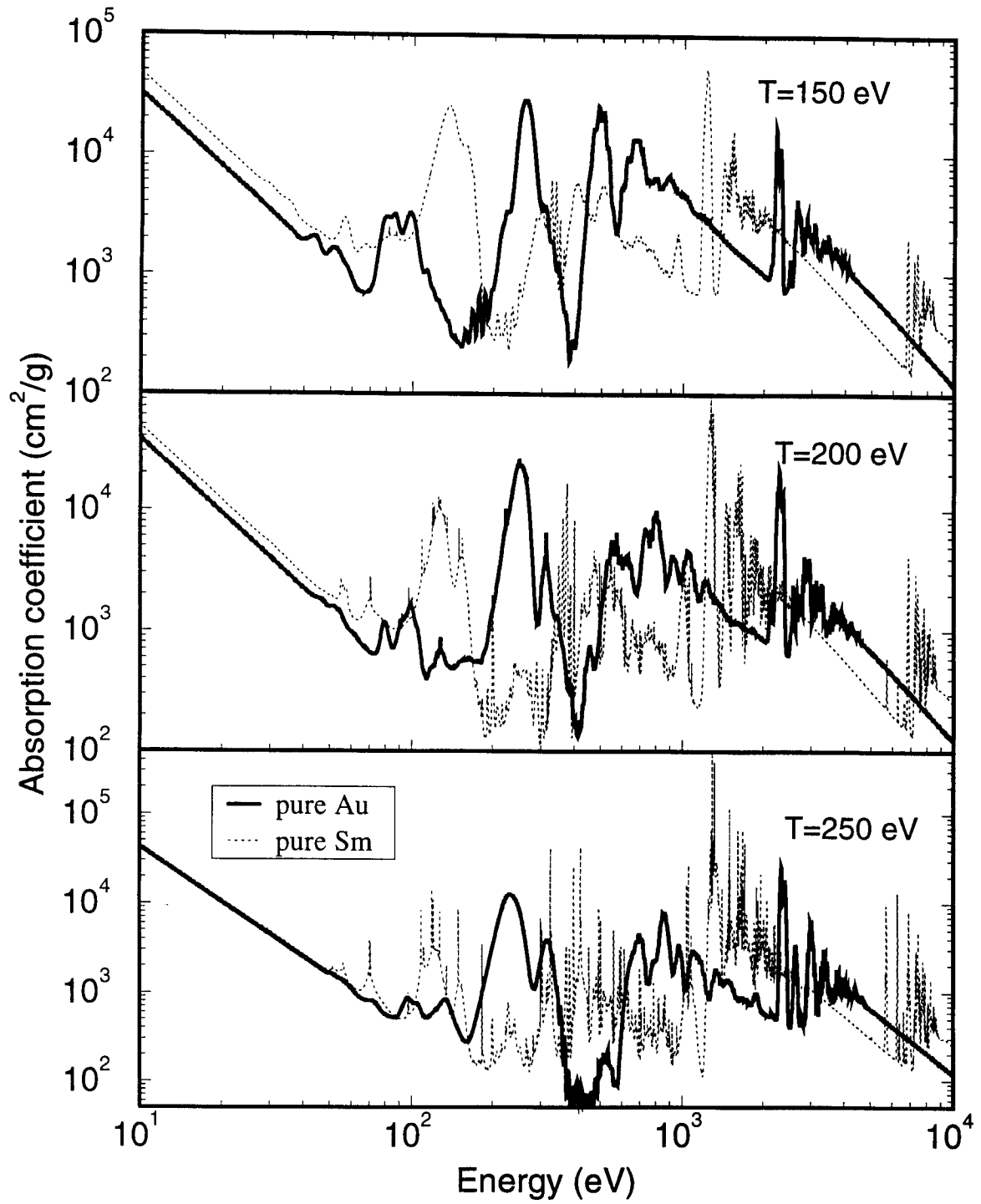


Figure 2.11. Opacities for pure Au and Sm at a density of 0.1 g/cm<sup>3</sup> and three different temperatures.

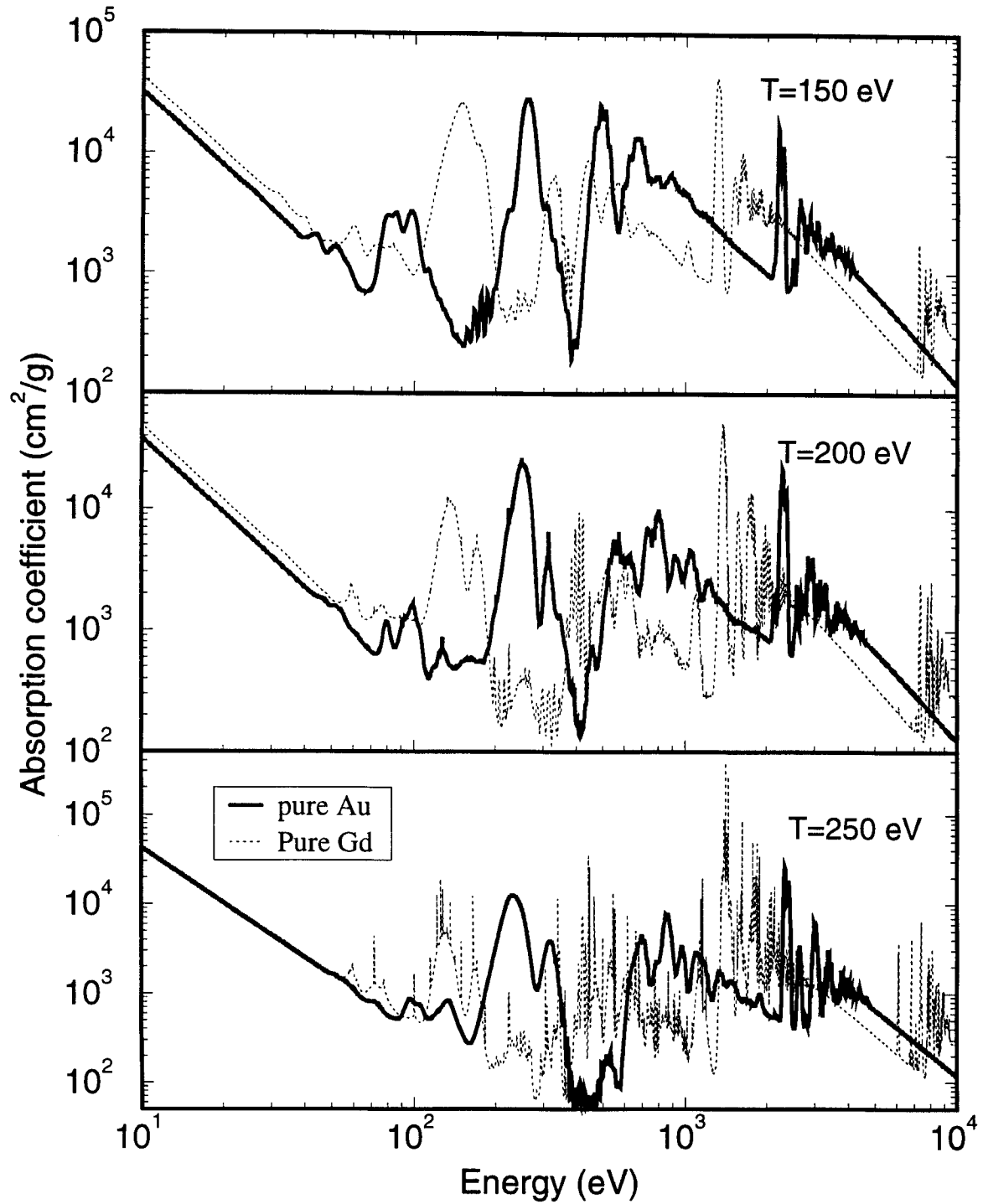


Figure 2.12. Opacities for pure Au and Gd at a density of  $0.1 \text{ g/cm}^3$  and three different temperatures.

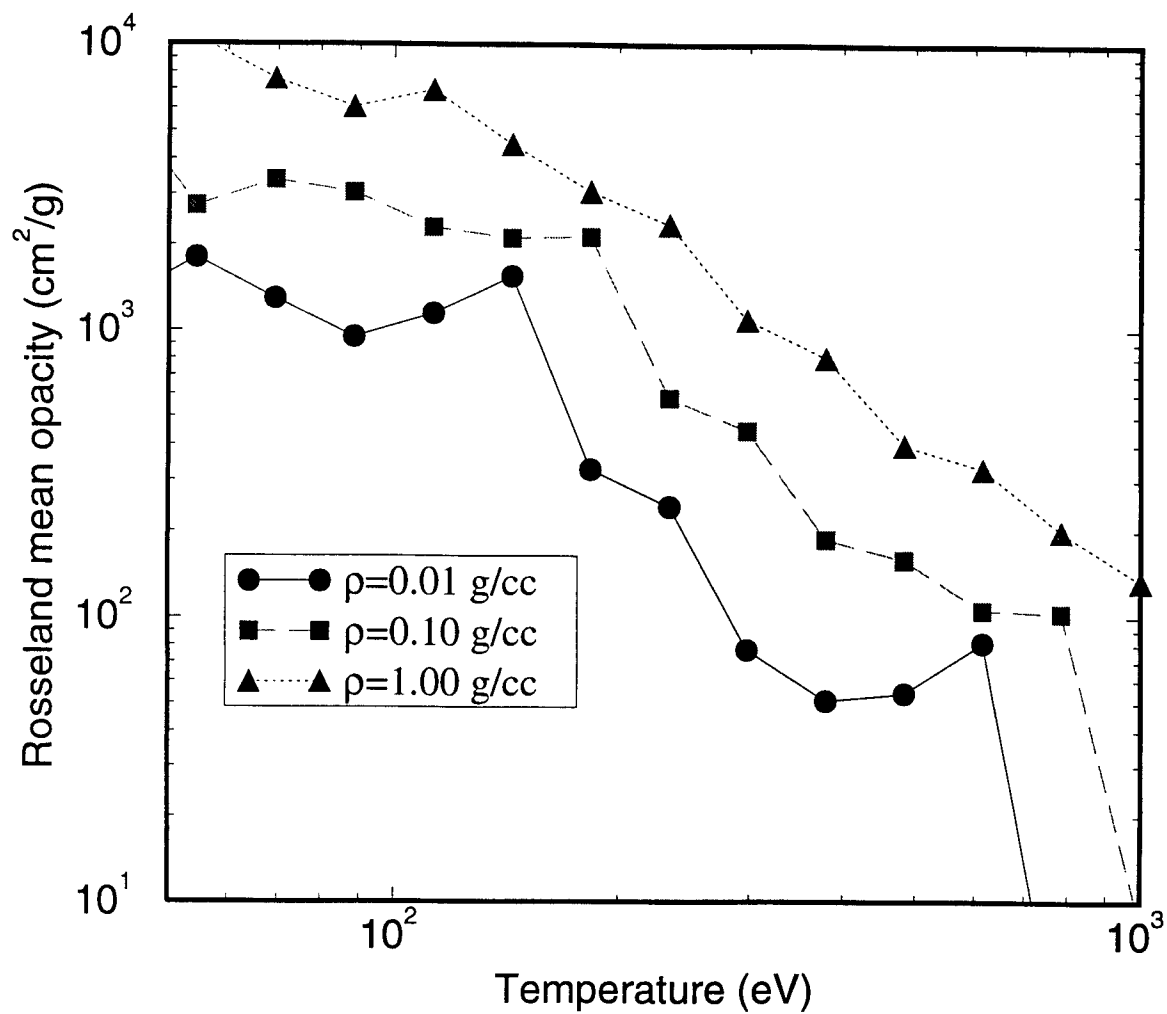


Figure 2.13. Calculated Au Rosseland mean opacities as a function of temperature.

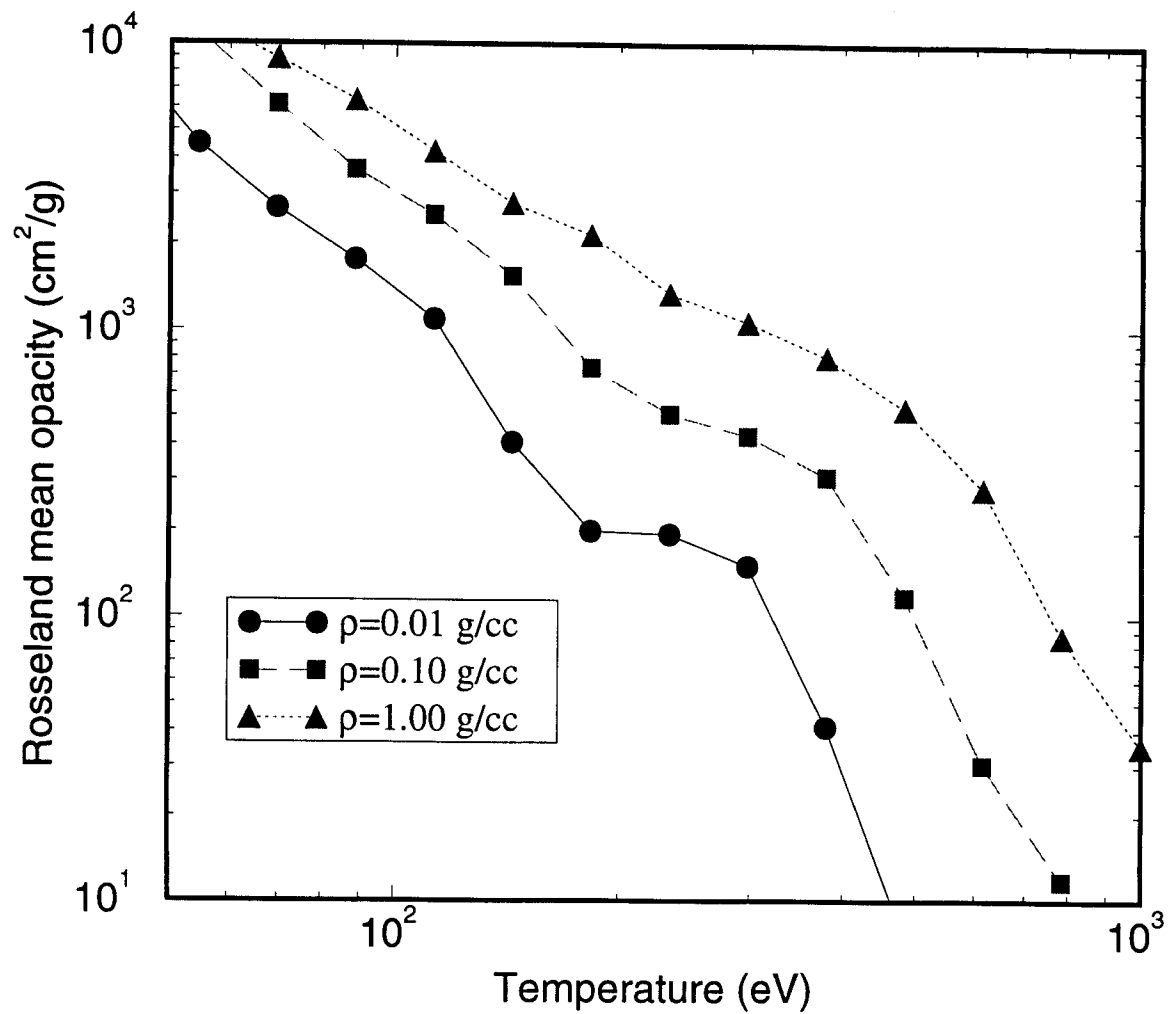


Figure 2.14. Calculated Sm Rosseland mean opacities as a function of temperature.

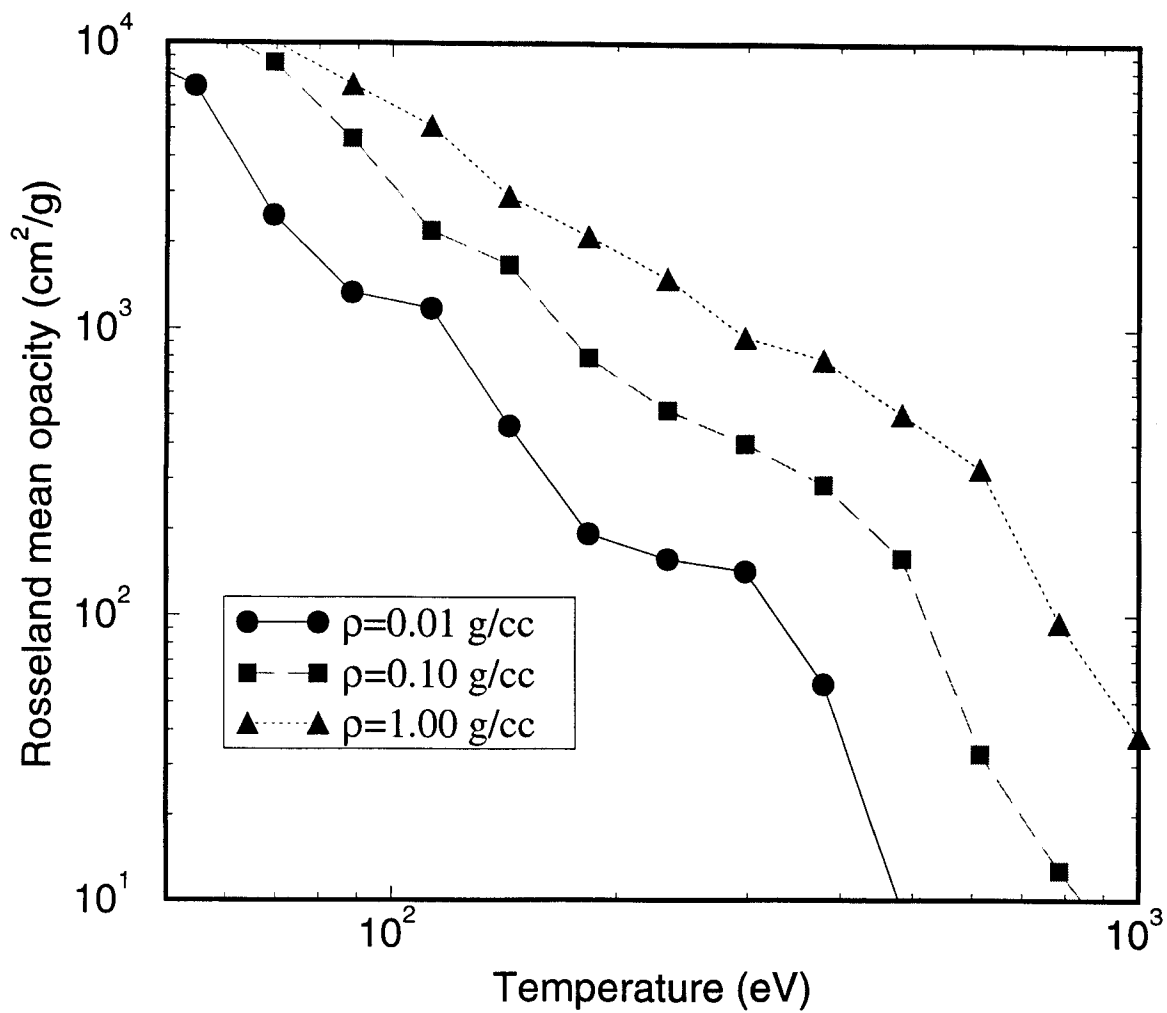


Figure 2.15. Calculated Gd Rosseland mean opacities as a function of temperature.

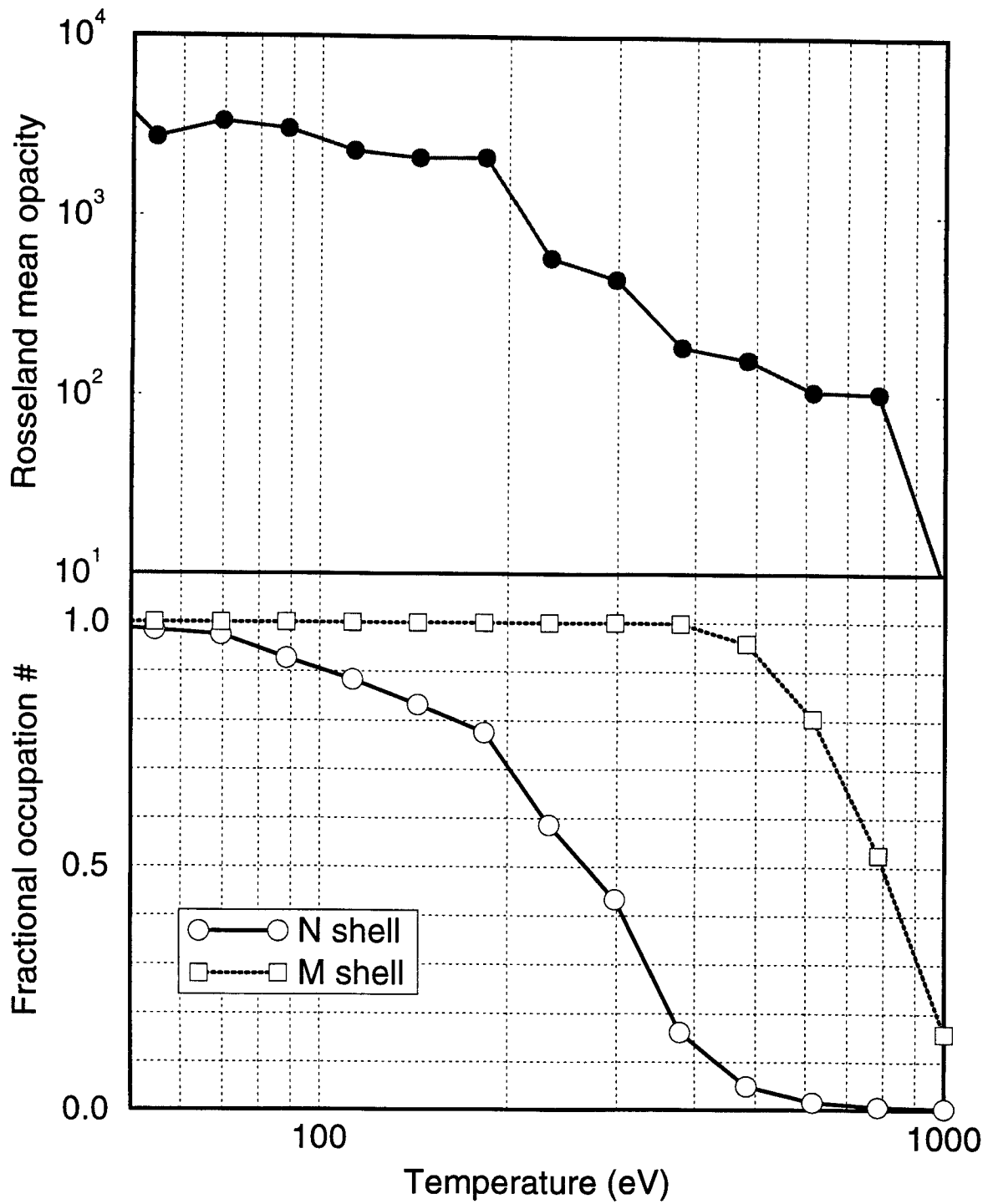


Figure 2.16. The effect of M- and N-shell electron populations on the Rosseland mean opacity. (Top) The Rosseland mean opacity of Au at a density of 0.1 g/cm<sup>3</sup>. (Bottom) Fractional M- and N-shell electron population number scaled to number of electrons of the closed shell.

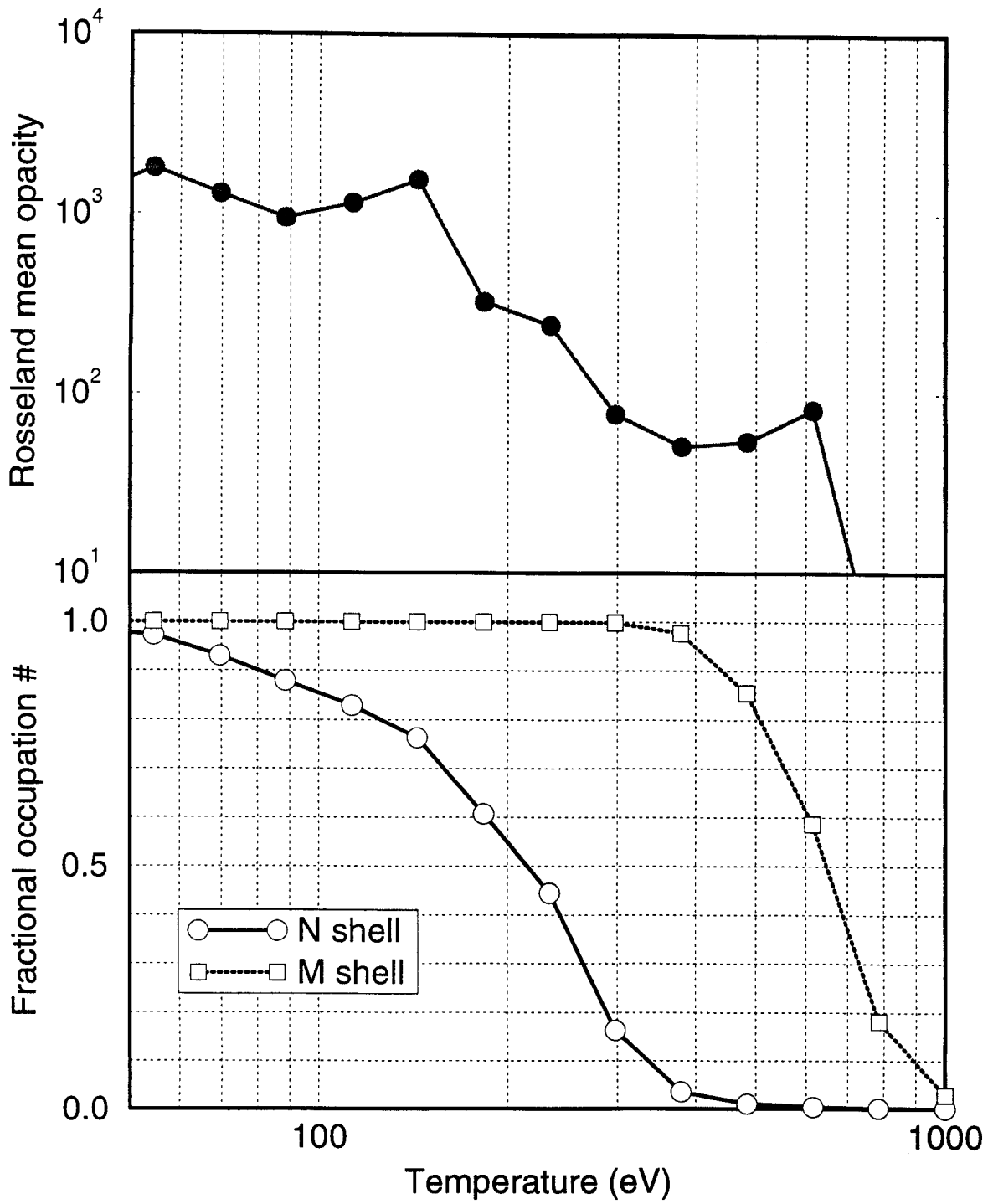


Figure 2.17. The effect of M- and N-shell electron populations on the Rosseland mean opacity. (Top) The Rosseland mean opacity of Au at density of 0.01 g/cm<sup>3</sup>. (Bottom) Fractional M- and N-shell electron population number scaled to number of electrons of the closed shell.

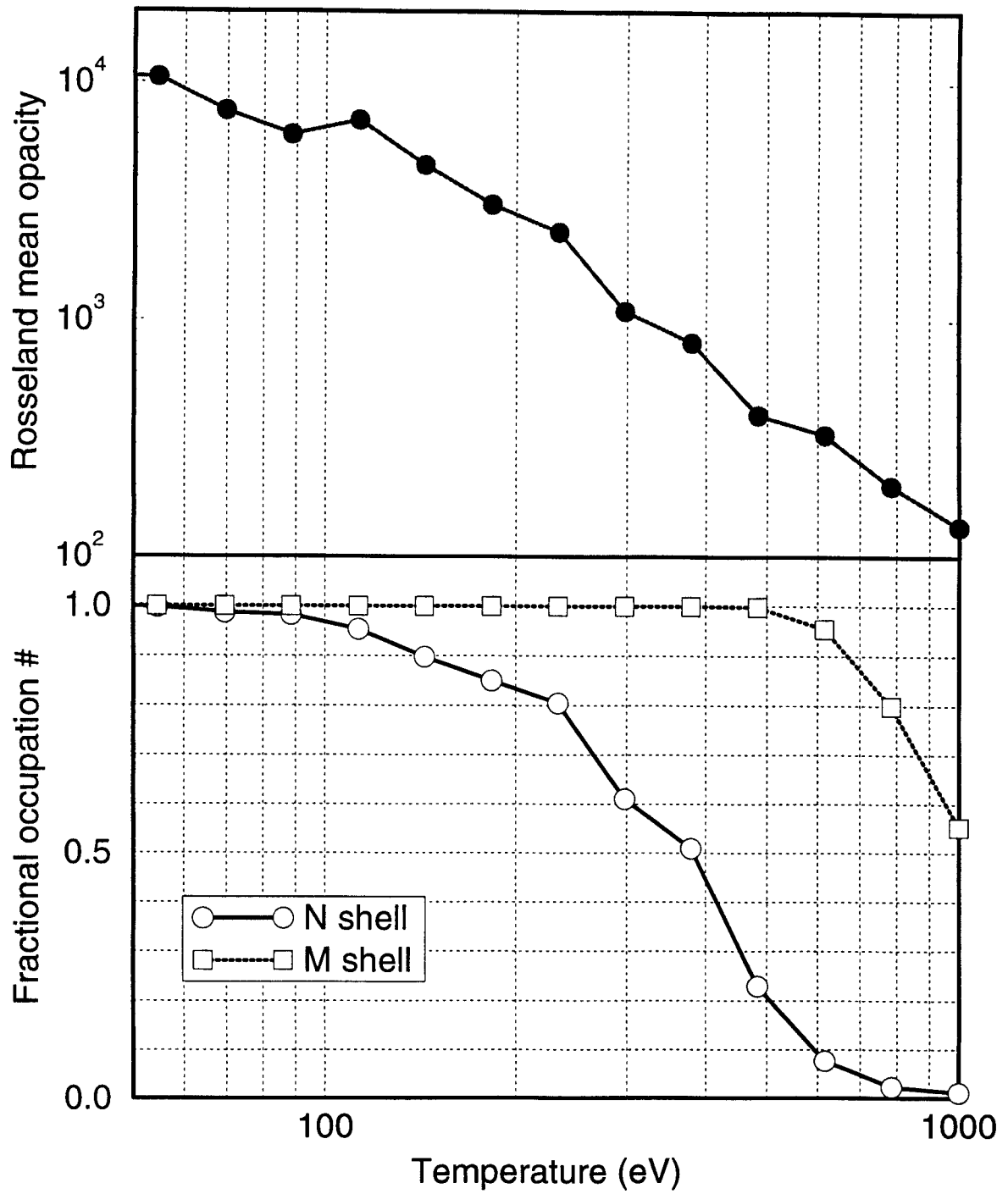


Figure 2.18. The effect of M- and N-shell electron populations on the Rosseland mean opacity. (Top) The Rosseland mean opacity of Au at a density of  $1.0 \text{ g/cm}^3$ . (Bottom) Fractional M- and N-shell electron population number scaled to number of electrons of the closed shell.

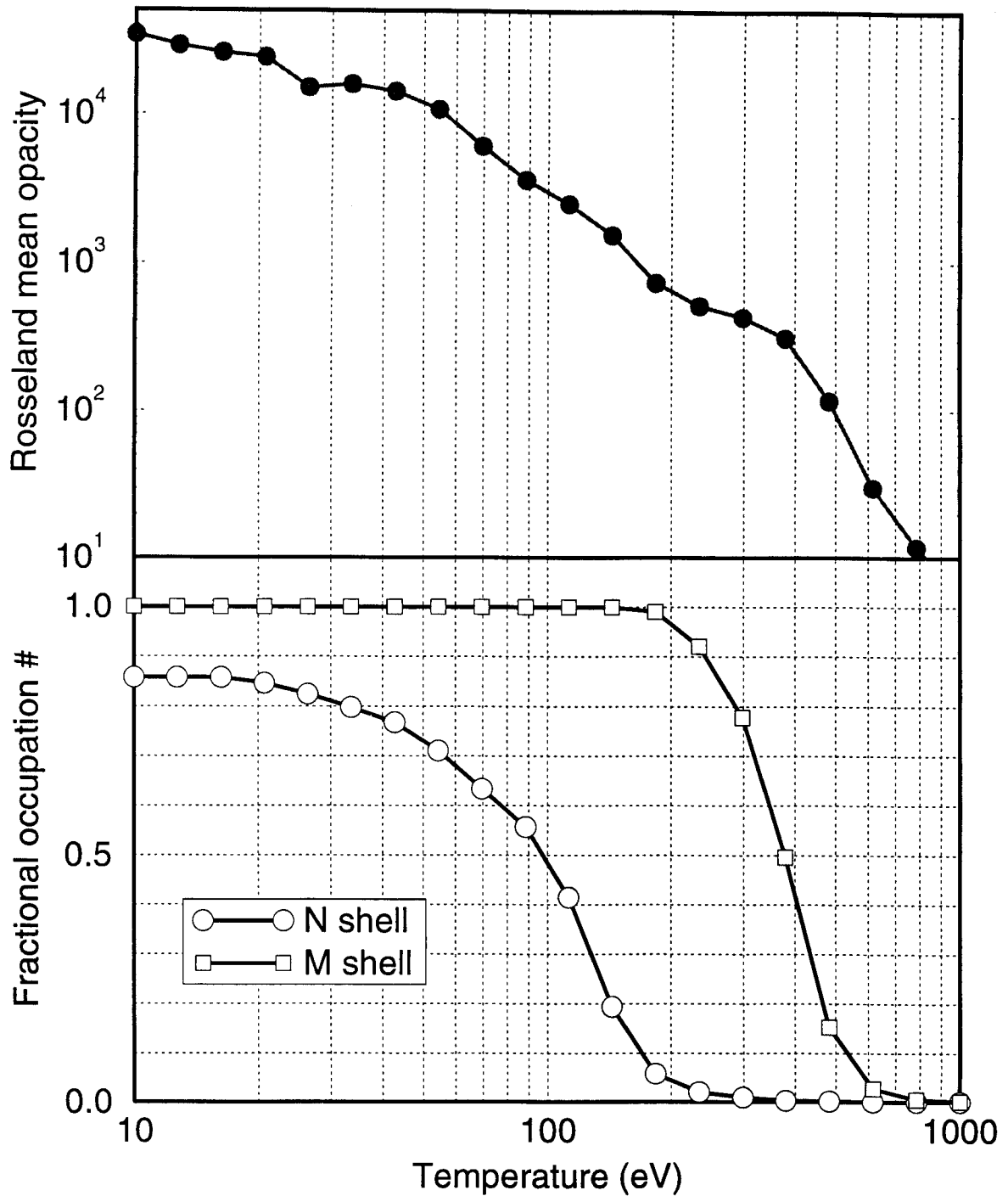


Figure 2.19. The effect of M- and N-shell electron populations on the Rosseland mean opacity. (Top) The Rosseland mean opacity of Sm at a density of  $0.01 \text{ g/cm}^3$ . (Bottom) Fractional M- and N-shell electron population number scaled to number of electrons of the closed shell.

Similarly, the second plateau near  $T = 700$  eV in Au and the plateaus near  $T = 300$  eV in Sm (Fig. 2.19) and Gd are caused by the strong M-band absorption. The Rosseland mean plateaus of Sm and Gd lay between the two plateaus of Au, suggesting that a mixture of Au with Sm or Gd can produce an enhancement on the Rosseland mean opacity in a manner which is dependent on temperature. For Au plasmas at densities of  $1.0 \text{ g/cm}^3$  or higher, the depopulation processes of the N- and M-shell electrons occur at higher temperatures. In such cases, the strong N- and M-band absorption features appear over a wider temperature range, and therefore the Rosseland mean opacity plateaus are not as obvious as those of lower density cases.

### 3. The Opacity of High-Z Mixtures

In calculating opacities for high-Z mixtures, we compute the equilibrium occupation numbers by solving the Saha equation including all the levels of both species in the mixture. Thus, plasma effects on both elements are consistent with the conditions of the mixture plasma.

Figure 3.1 shows calculated absorption coefficients for Au, Sm, and a Au-Sm mixture with a 1:1 particle number mixing ratio at  $T = 225$  eV and  $\rho = 0.1$  g/cm<sup>3</sup>. It can be seen that the major absorption peaks of Sm ( $n = 3 \rightarrow n > 3$  near 1-2 keV and  $n = 4 \rightarrow n > 4$  near 0.3-0.7 keV) nicely fill in the two major absorption valleys of gold. In this particular case, we find almost a factor of two increase in the Rosseland mean opacity.

To study the opacity enhancement effect of high-Z mixtures, we have performed a series of opacity calculations for mixtures of Au-Sm and Au-Gd with various mixing ratios over a range of temperature and density conditions relevant to ICF hohlraums. Some typical results are shown in Fig. 3.2. In this figure, the Rosseland mean opacities for Au-Sm and Au-Gd mixtures are plotted as a function of the fractional number density of gold at the density of 0.1 g/cm<sup>3</sup>, and at four different temperatures ranging from 150 eV to 300 eV. It is seen that the Rosseland mean opacity is significantly enhanced in the Au-Sm and Au-Gd mixtures. Note also that the enhancements are sensitive to the plasma temperatures. In particular, the enhancement increases significantly with temperature between  $T = 200$  eV and 300 eV.

This temperature dependence can be seen more clearly from Figs. 3.3 and 3.4, where the Rosseland mean opacities of Au, Sm, Gd, and mixtures of Au-Sm and Au-Gd are shown as a function of temperature. Note that the mixtures produce the strongest enhancements in the Rosseland mean in the temperature range between two plateaus of Au; i.e., just above  $T \approx 200$  eV, where the Rosseland mean opacity exhibits a significant drop.

Our calculations also show that the Rosseland mean opacity enhancement effect of mixtures is less significant for higher density plasmas. This is because higher densities tend to depress ionization states of plasmas. For a Au plasma at  $T = 250$  eV and  $\rho = 0.01$  g/cc, the average charge state is about 45, with more than 75% of N-shell electrons being ionized. The absorption features arising from 4*d* and 4*f* electrons become very weak, which therefore leads to a distinct absorption valley around  $h\nu \approx 500$  eV and a dramatic decrease in the Rosseland mean opacity. The N-band absorption features of Sm and Gd fill in this valley; hence the Rosseland mean opacity is significantly enhanced in the Au/Sm and Au/Gd

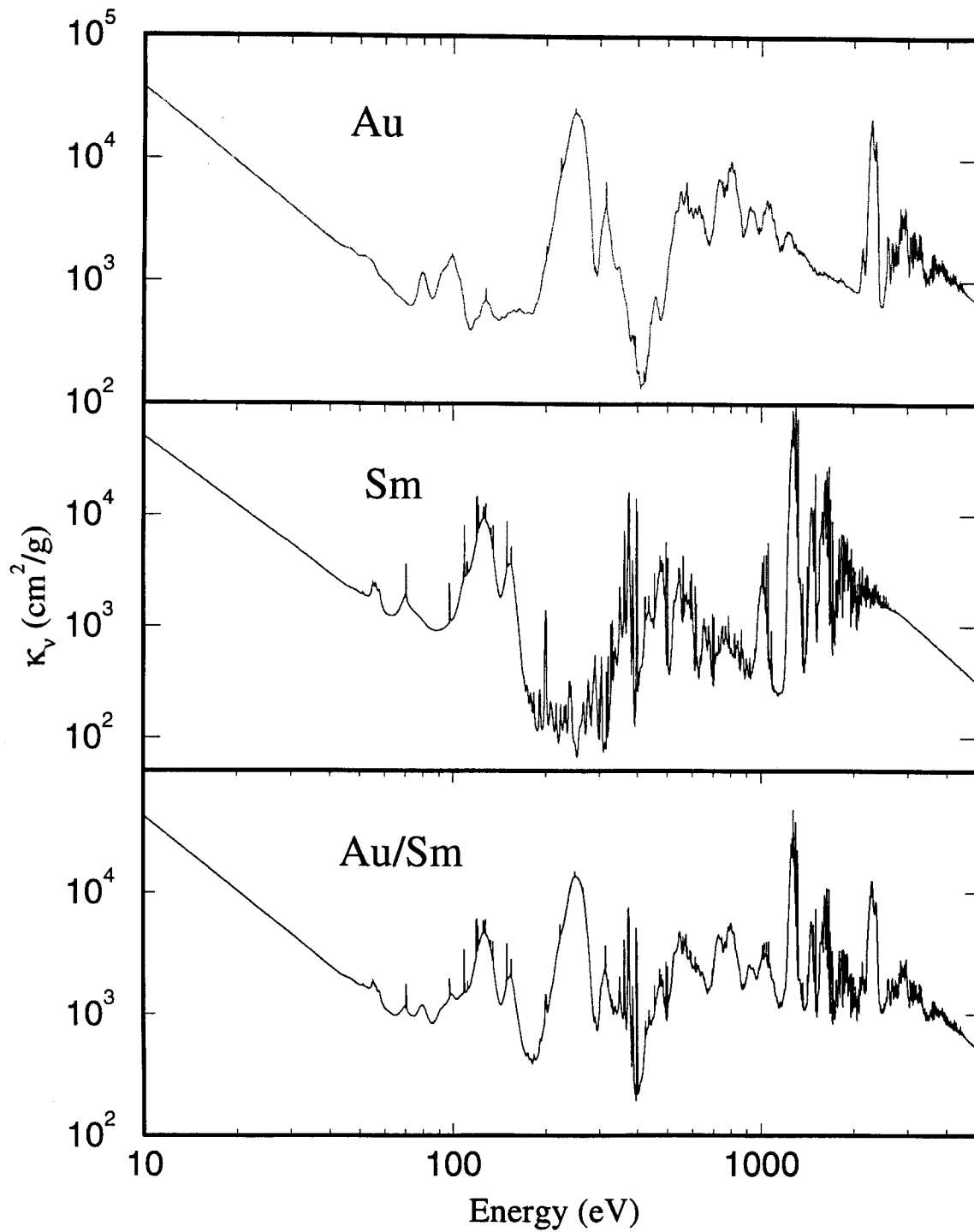


Figure 3.1. Calculated opacities for Au, Sm, and a Au-Sm mixture at  $T = 225$  eV,  $\rho = 0.1$   $\text{g}/\text{cm}^3$ . The particle number mixing ratio for Au-Sm is 1:1.

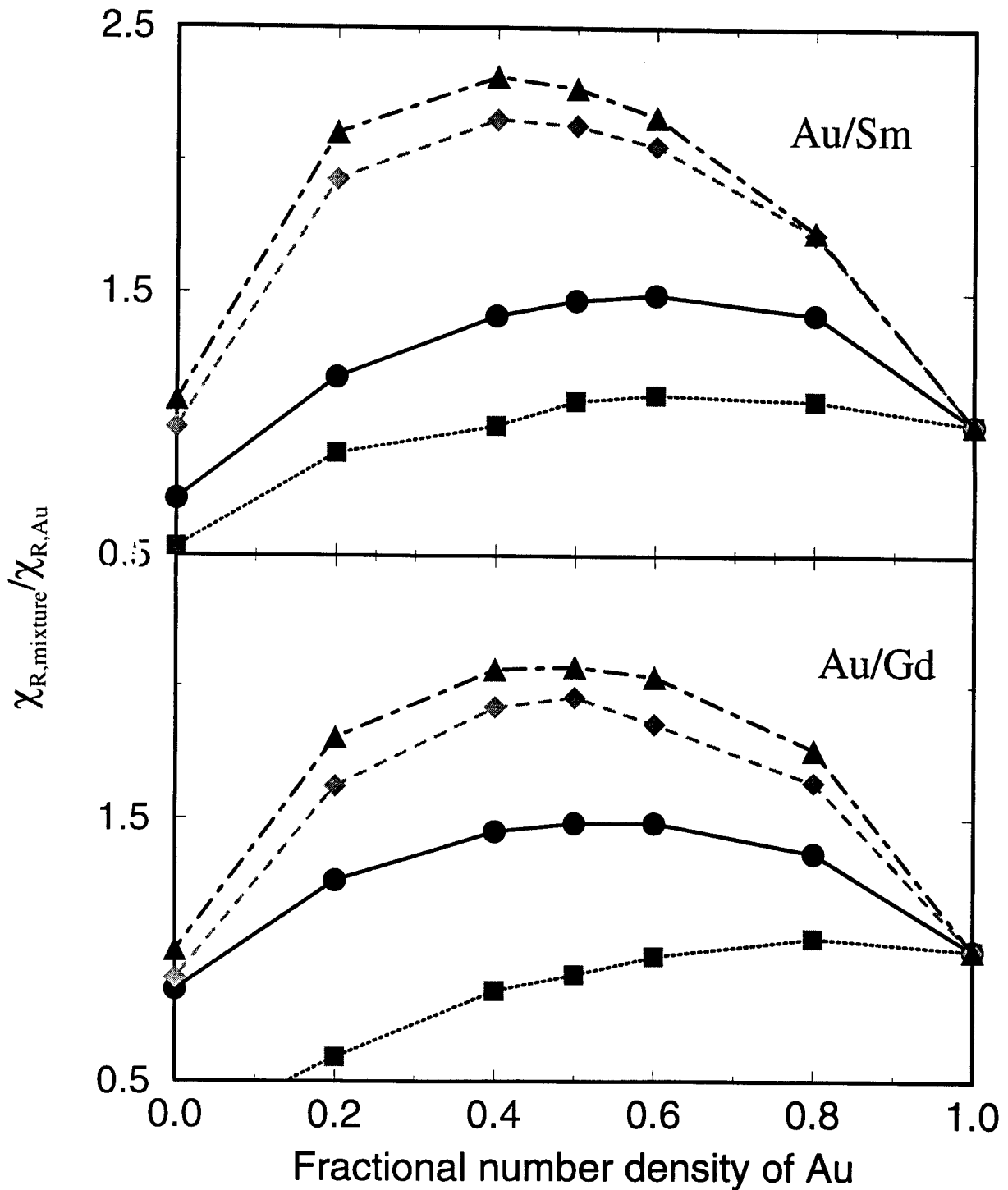


Figure 3.2. Calculated Rosseland mean opacity for Au-Sm and Au-Gd mixtures vs. fractional number density of gold. The density of the mixtures for both Au-Sm and Au-Gd is  $0.1 \text{ g/cm}^3$ . Results at four different temperatures are shown. The Rosseland mean opacities for mixtures are scaled to the corresponding Au values:  $T = 150 \text{ eV}$  (circles),  $\chi_{R,Au} = 2158 \text{ cm}^2/\text{g}$ ;  $T = 200 \text{ eV}$  (squares),  $\chi_{R,Au} = 1045 \text{ cm}^2/\text{g}$ ;  $T = 250 \text{ eV}$  (diamonds),  $\chi_{R,Au} = 570 \text{ cm}^2/\text{g}$ ; and  $T = 300 \text{ eV}$  (triangles),  $\chi_{R,Au} = 440 \text{ cm}^2/\text{g}$ .

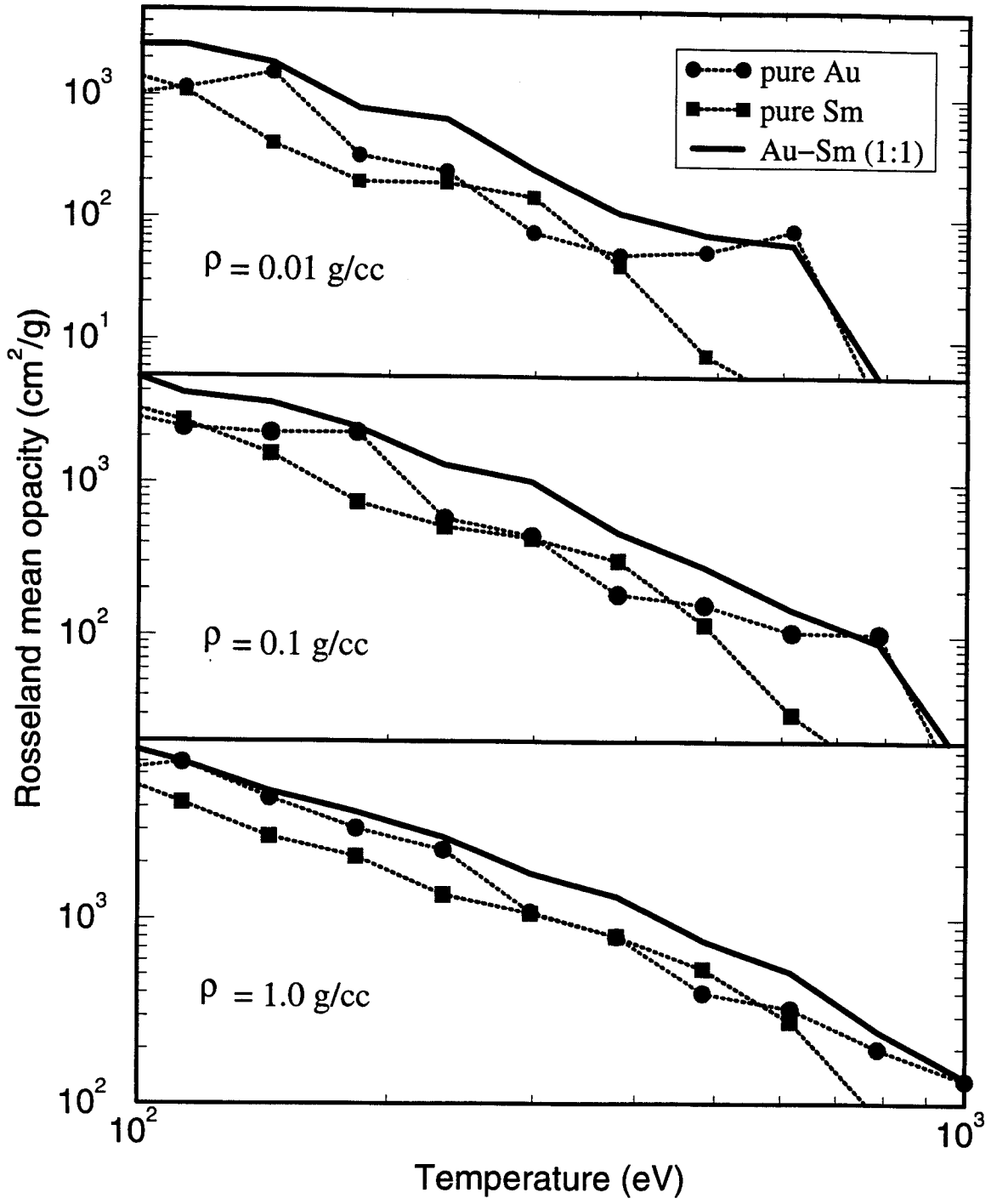


Figure 3.3. Calculated Rosseland mean opacities for an Au, Sm, and Au-Sm mixture as a function plasma temperature at three different densities. The particle number mixing ratio for the Au-Sm mixture is 1:1.

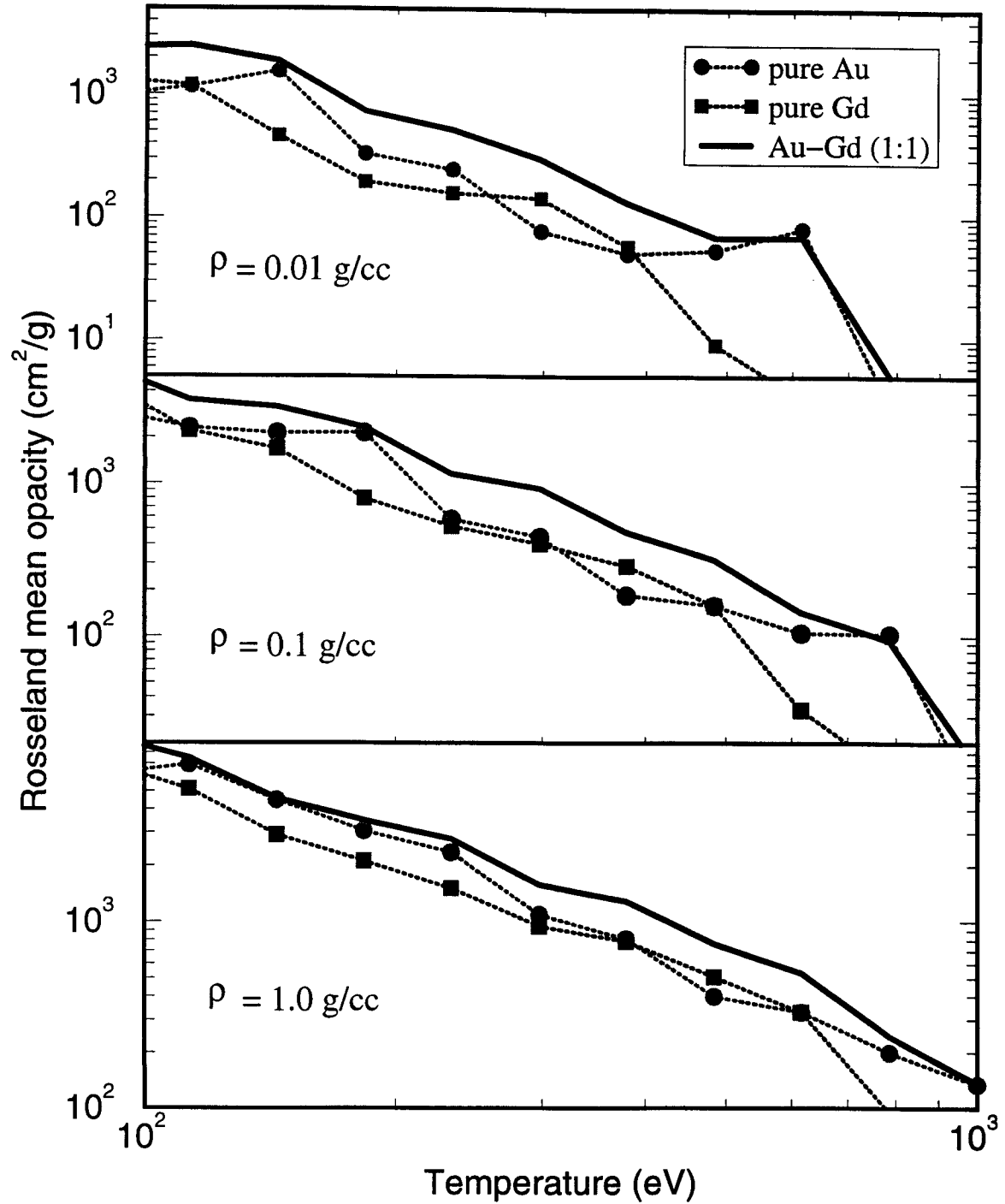


Figure 3.4. Calculated Rosseland mean opacities for Au, Gd, and an Au-Gd mixture as a function plasma temperature at three different densities. The particle number mixing ratio for the Au-Gd mixture is 1:1.

mixtures for these conditions. For a Au plasma at  $T = 250$  eV and  $\rho = 1$  g/cc, however, the average charge state is about 30, with an almost fully populated N shell. In this case, the contribution from Sm or Gd does not provide a significant enhancement. This is shown more clearly in Figs. 3.5 and 3.6, where the relative contribution due to different frequency regions is shown. Here, the results for a pure Au plasma at a density of  $1$  g/cm<sup>3</sup> are compared with those of an Au/Sm mixture. It can be seen that even though the mixture fills in the two absorption valleys of Au to some degree, the lower absorption near  $h\nu \approx 0.6 - 1.1$  keV leads to a Rosseland mean opacity which is about the same for the two cases. In this particular case, the mixture has about a ten percent enhancement in the Rosseland mean opacity.

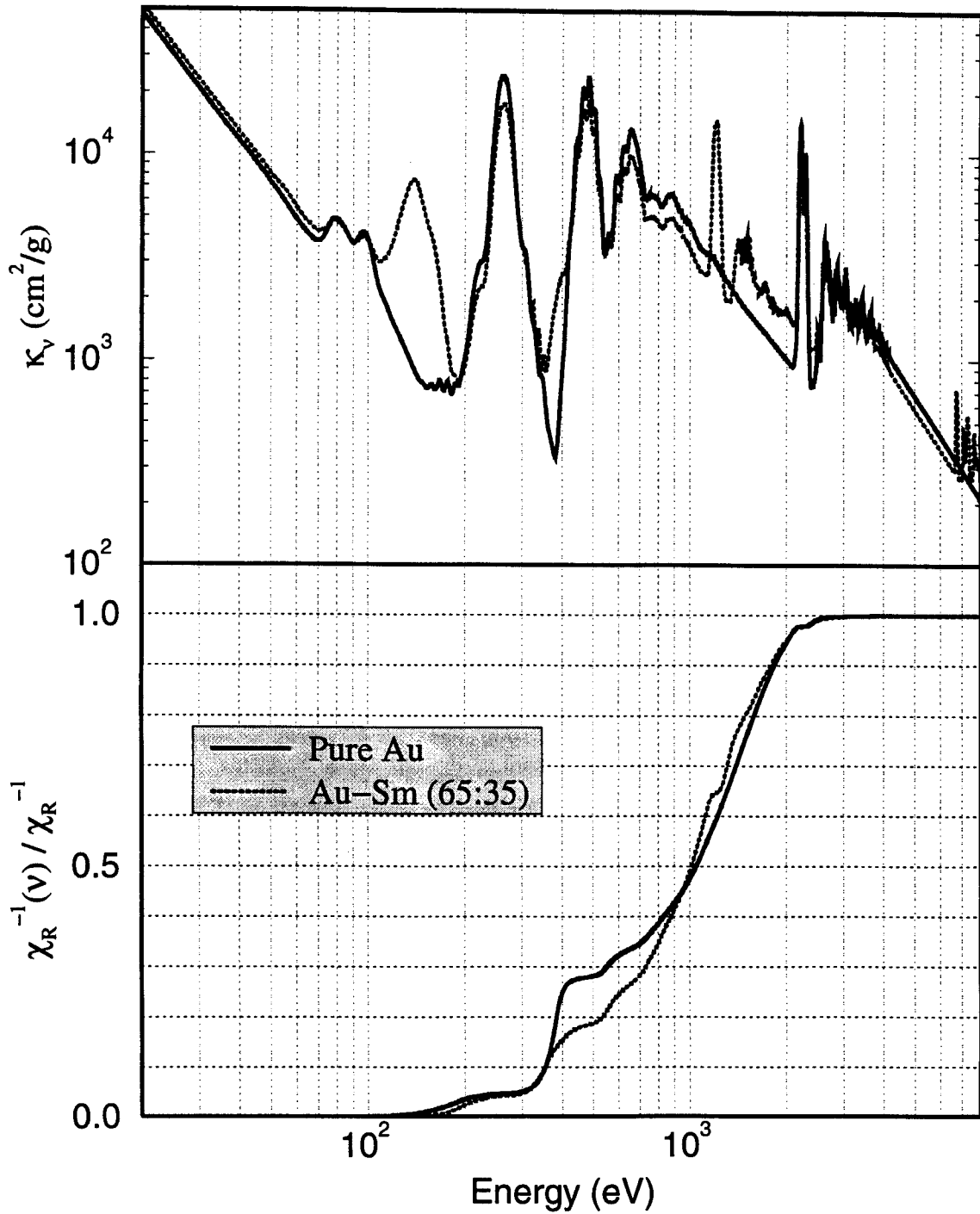


Figure 3.5. (Top) Calculated absorption coefficients for pure Au and a 65:35 Au-Sm mixture at  $T = 200$  eV,  $\rho = 1$  g/cm<sup>3</sup>. (Bottom) Relative cumulative contribution to the Rosseland mean opacity as a function of frequency.

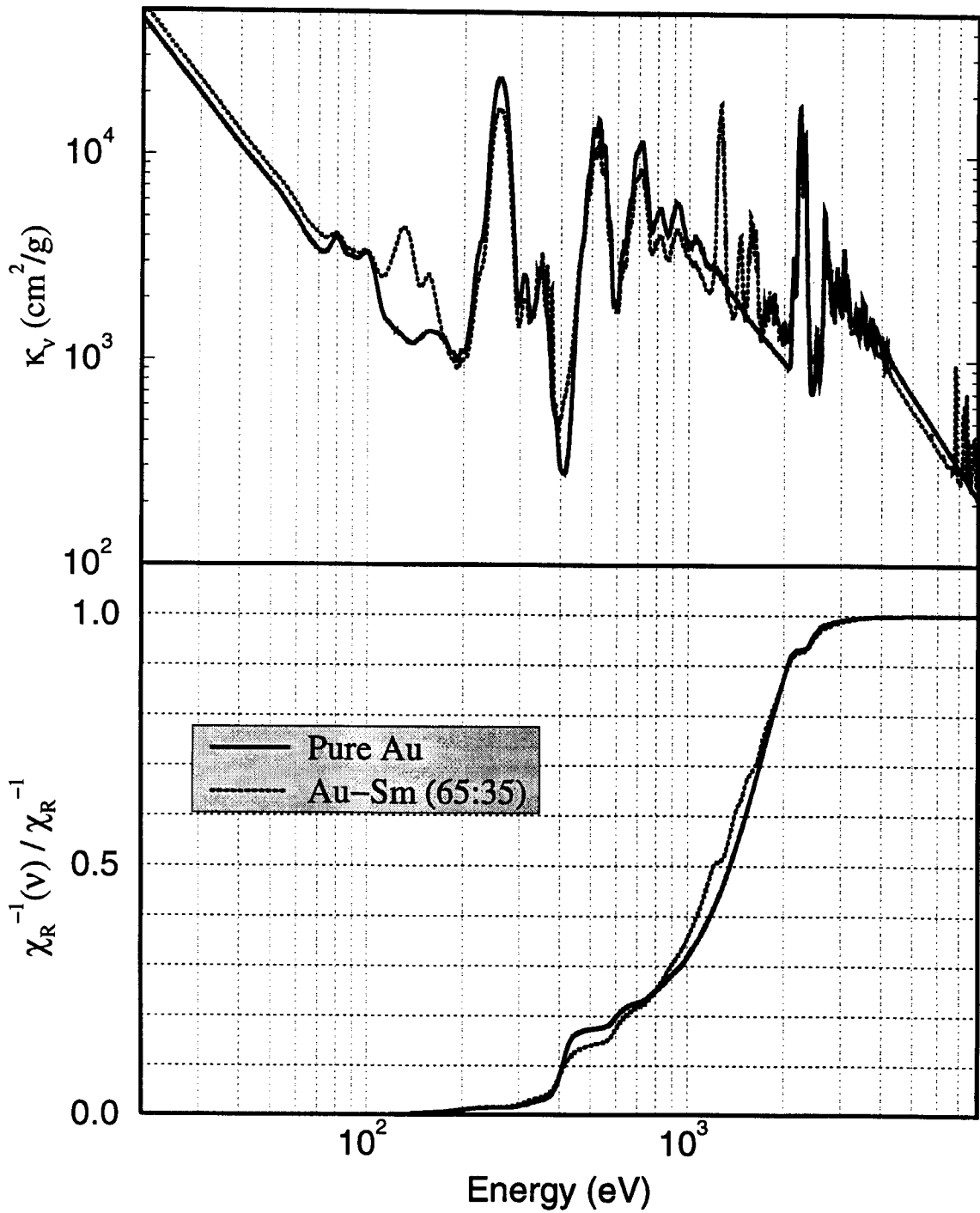


Figure 3.6. (Top) Calculated absorption coefficients for pure Au and a 65:35 Au-Sm mixture at  $T = 250$  eV,  $\rho = 1$  g/cm<sup>3</sup>. (Bottom) Relative cumulative contribution to the Rosseland mean opacity as a function of frequency.

## 4. Radiation Burnthrough Simulations for High-Z Mixtures

Using the high-Z opacities discussed in the preceding sections of this report, we have performed radiation burnthrough simulations for pure Au, Gd, and Sm samples, as well as Au-Gd and Au-Sm mixtures. The simulations were carried out using BUCKY-1, a 1-D radiation-hydrodynamics code [7]. A summary of the foil characteristics used in the simulations is given in Tables 4.1 and 4.2. Listed are the number fraction of either Gd or Sm, the sample thickness, the initial density, and the areal mass density. The density of the mixtures  $\bar{\rho}$  was determined from the relation:

$$\frac{\bar{A}}{\bar{\rho}} = \sum_i (x_i A_i / \rho_i),$$

where

$$\bar{A} = \sum_i x_i A_i$$

is the mean atomic weight, and  $x_i$ ,  $A_i$ , and  $\rho_i$  are the atomic number fraction, atomic weight, and density of the pure species  $i$ . The thicknesses listed for the 0%, 34%, and 63% Gd cases were taken to be those of the samples used in the NOVA experiments. In all other cases, the thickness were chosen to give an areal mass density equal to that of the pure Au case.

The radiation-hydrodynamics simulations were carried out in planar geometry. BUCKY-1 is a 1-D Lagrangian hydrodynamics code, which solves a single-fluid equation of motion with pressure contributions from electrons, ions, and radiation. Energy transport in the plasma can be treated using either a one-temperature ( $T_i = T_e$ ) or two-temperature  $T_i \neq T_e$  model. Both the electrons and ions are assumed to have a Maxwellian distribution defined by  $T_i$  and  $T_e$ . Shocks are modeled using a von Neumann artificial viscosity. Thermal conduction is treated using Spitzer conductivities, with the electron conduction being flux-limited.

Radiation emission and absorption terms are coupled to the electron temperature equation. BUCKY-1 has several options for calculating multifrequency radiation intensities. In most of the calculations discussed below, an integral radiation transport model based on the method of short characteristics was used. In calculations in which a laser deposition simulation was carried to assess the effects of a non-Planckian spectrum on the results, a radiation diffusion model was used. A total of 100 frequency groups was used in the simulations. In most of the simulations, the incident radiation field onto the sample was taken to be a Planckian spectrum defined by a time-dependent radiation temperature  $T_R(t)$  (see Fig. 4.1). The geometry for this type of calculation is illustrated in Fig. 4.2(a). More

**Table 4.1. Burnthrough Sample Characteristic for Au-Gd Mixtures**

% Gd	$\Delta L(\mu\text{m})$	$\rho_0$ (g/cm <sup>3</sup> )	$\rho_0 \Delta L$ (mg/cm <sup>2</sup> )
0	1.60	19.3	3.09
34	2.22	13.5	2.99
63	3.00	10.5	3.16
100	3.93	4.89	3.09

**Table 4.2. Burnthrough Sample Characteristic for Au-Sm Mixture**

% Sm	$\Delta L(\mu\text{m})$	$\rho_0$ (g/cm <sup>3</sup> )	$\rho_0 \Delta L$ (mg/cm <sup>2</sup> )
0	1.60	19.3	3.09
50	2.68	11.5	3.09
100	4.15	7.54	3.09

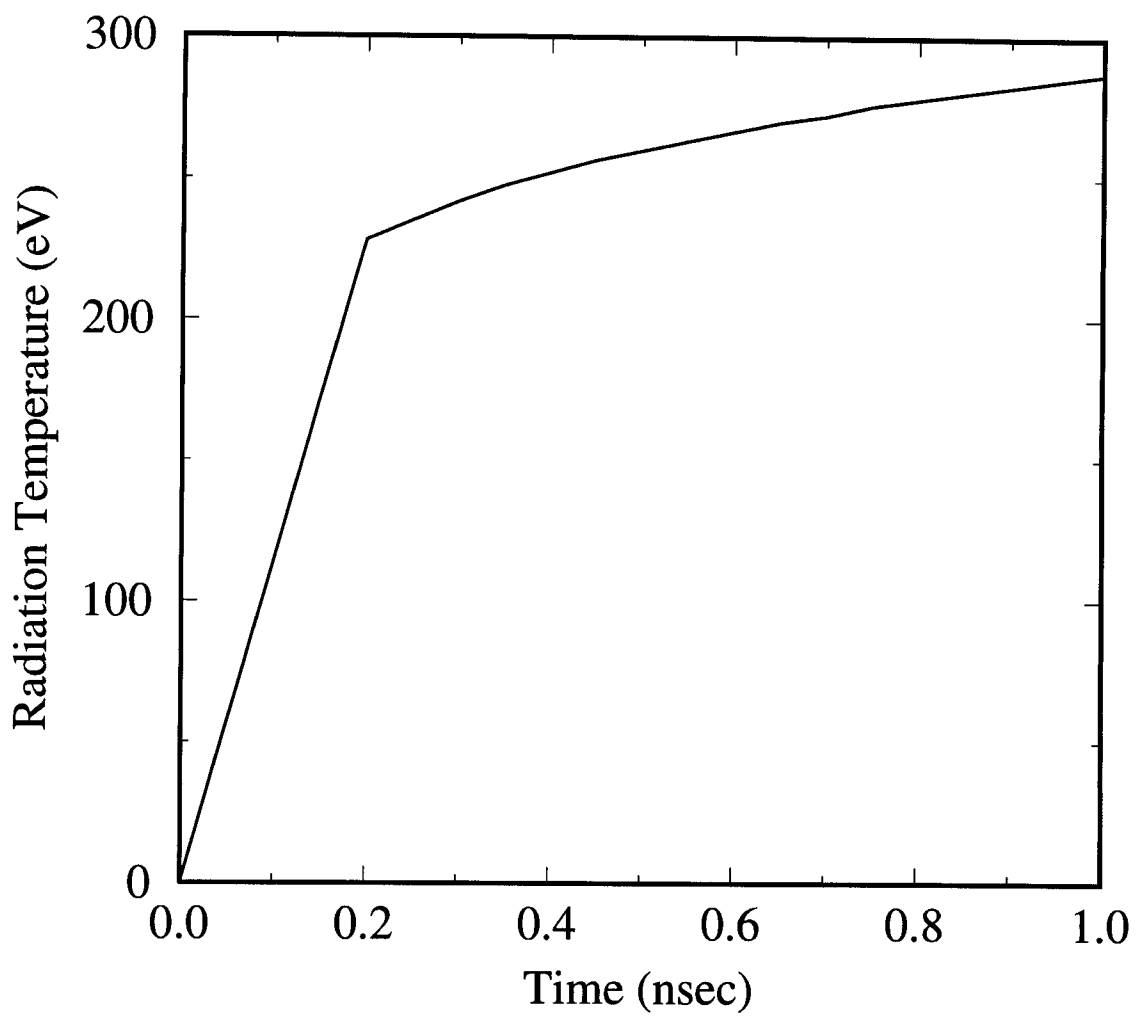


Figure 4.1. Time-dependent radiation temperature at the front-side boundary.

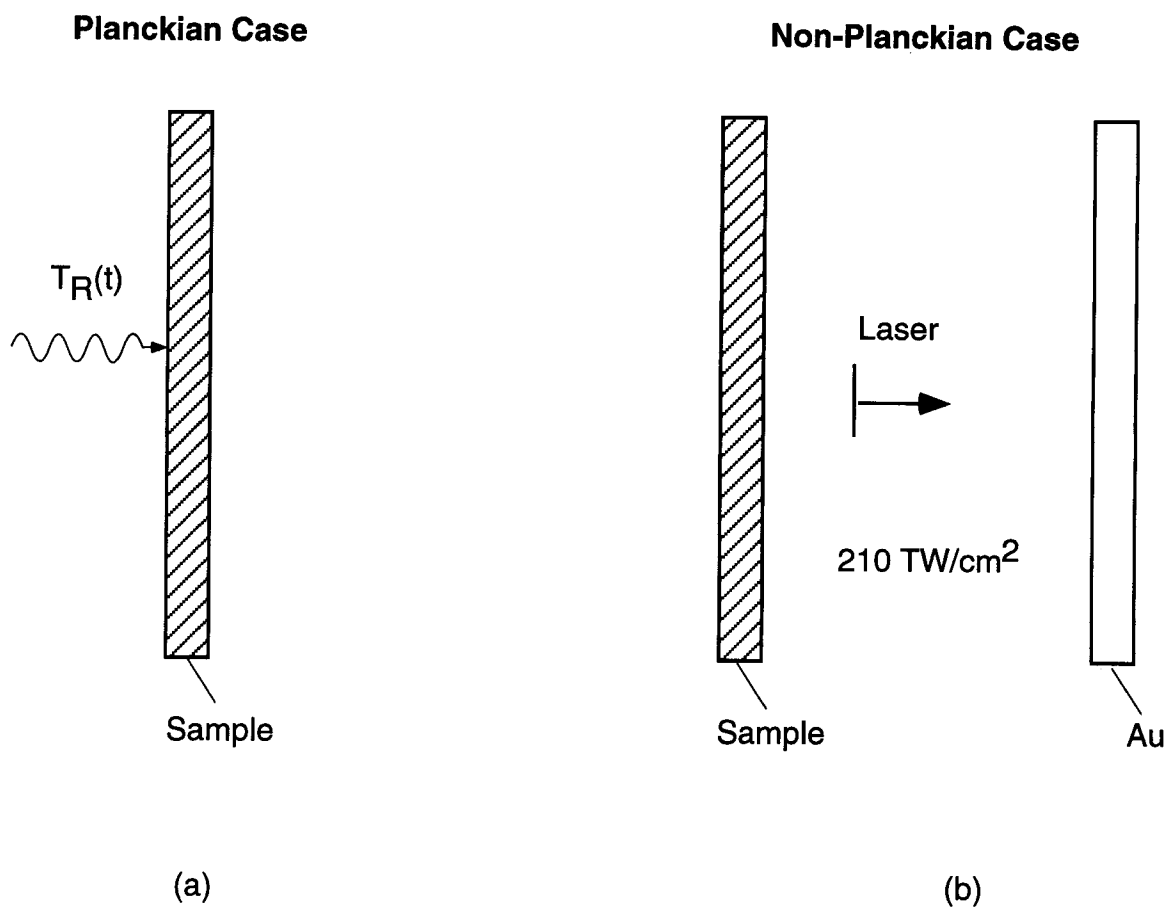


Figure 4.2. (a) Schematic illustration of a single-foil geometry with an incident Planckian spectrum. (b) A two-foil geometry in which a non-Planckian radiation field is established by the deposition of laser energy.

recently, we have performed simulations using a two-foil geometry (Fig. 4.2(b)). In this case, laser light originates at the midpoint between a gold foil and the sample. The laser is pointed at the Au foil. The deposition of laser light occurs via inverse Bremsstrahlung, with a dump of the remaining energy at the critical density. In these simulations, electron temperatures of between 1 and 2 keV are generated, producing a radiation field on the sample which is non-Planckian.

Results for simulations for Au-Gd mixtures are presented in Figs. 4.3 and 4.4. Figure 4.3 shows the rear surface flux in the 250 eV channel as a function of time. Note that the burnthrough time is shortest for pure Gd because of its lower opacity. It is also clear that the burnthrough times for the 34% Gd and 63% Gd mixtures are longer than both the pure Au and pure Gd cases. This is due to the enhanced opacities of the mixtures (discussed in Section 3). Figure 4.3 shows that the burnthrough times in the simulations are about 40 ps and 60 ps longer for the 34% and 63% Gd cases, respectively, than that of the pure Au simulation. By comparison, the corresponding experimental data for these cases indicates delays in the burnthrough time of about 100 ps and 150 ps [8]. Thus, although our simulations are in qualitative agreement with the experimental data, the predicted delays in the burnthrough times are somewhat smaller than the experimental values.

Figure 4.4 shows the time dependence of the albedos in the Au-Gd simulations. At  $t \approx 0.6$  ns, the albedos of pure Gd and pure Au are about 0.629 and 0.737, respectively. Again, the 34% Gd and 63% Gd results do not lie between the pure species simulations, but show an enhancement of the albedo. This enhancement is predicted to be approximately 1 to 3 percent. However, since the delays in the burnthrough times are more pronounced in the experimental data, one might suspect the experimental results suggest albedo enhancements of a somewhat greater magnitude. Similar results for the Au-Sm mixtures are shown in Figs. 4.5 and 4.6. Again, the enhanced opacity of the 1:1 Au-Sm mixture leads to a longer burnthrough time than for either the pure Sm or pure Au cases (see Fig. 4.5). The delay relative to pure Au is about 70 ps. Figure 4.6 shows an enhancement of the albedo of approximately 0.03 relative to pure Au.

Although our simulations using the UTA mixture opacities behave qualitatively similar to the experimental data, the longer burnthrough times for the Gd-Au mixtures are less pronounced than in the experiments. One can then ask several questions in regards to the discrepancies. For example, how much more opacity is required from the mixture to produce burnthrough delay times which are consistent with the data? Could the discrepancy result

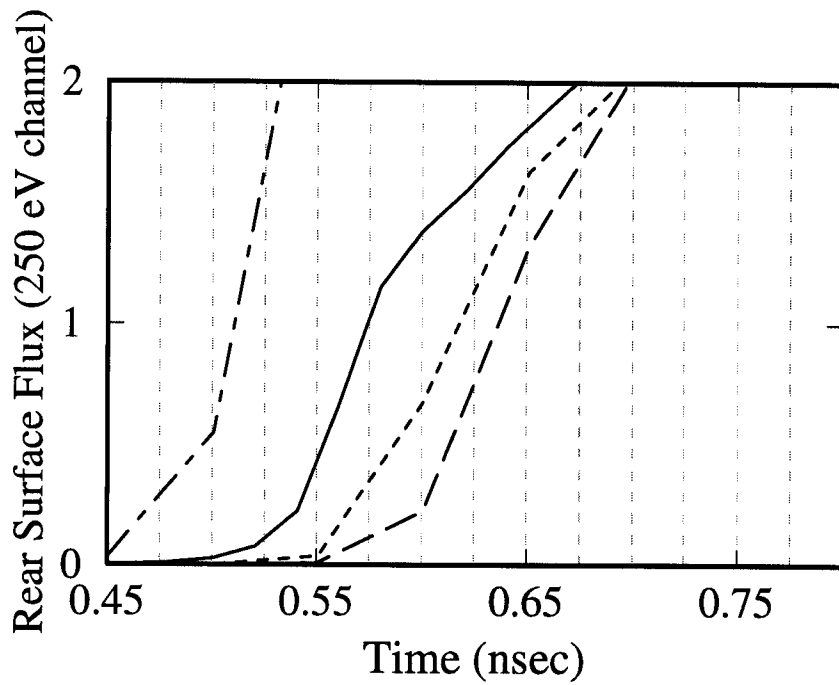
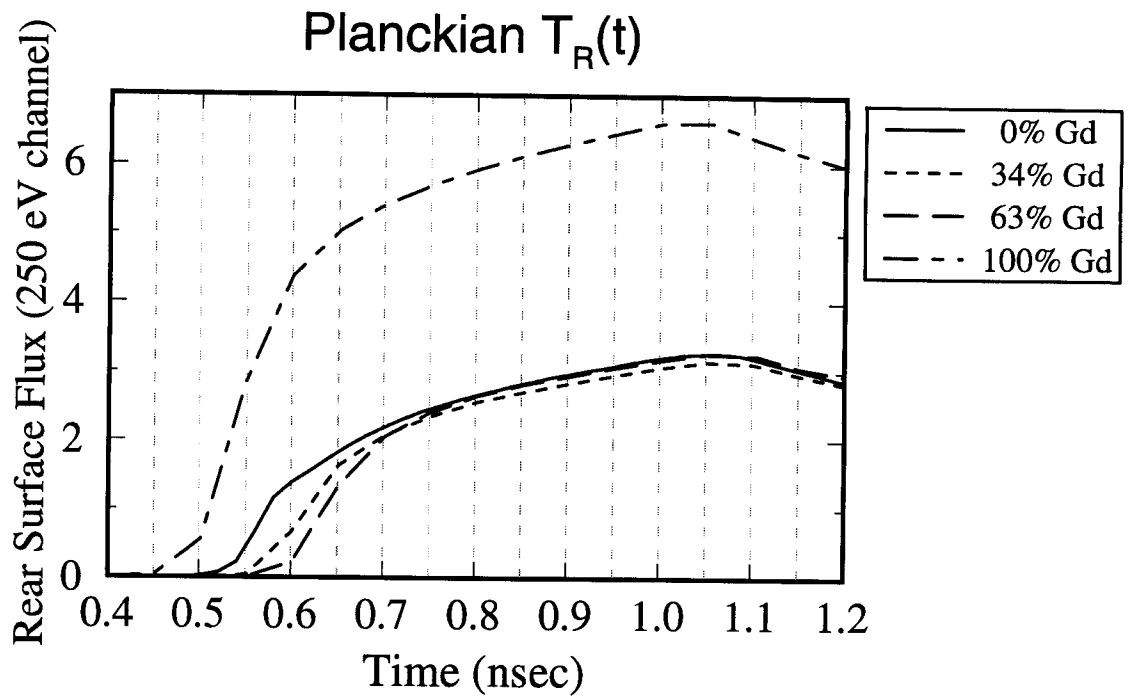


Figure 4.3. Time dependence of rear-side flux in the  $h\nu = 250$  eV band for Au-Gd radiation burnthrough simulations. The lower plot is the same as the upper plot, but on a different scale.

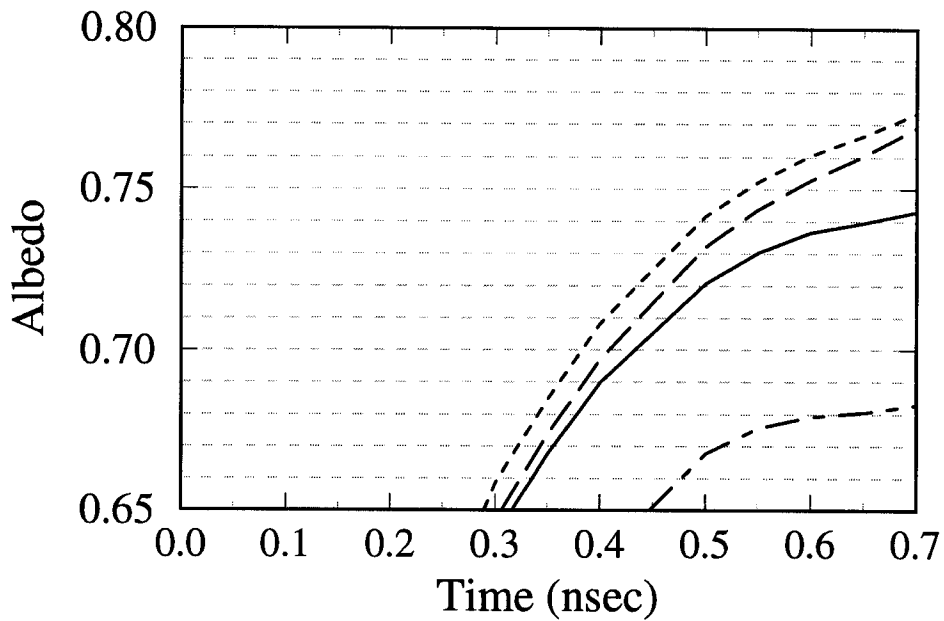
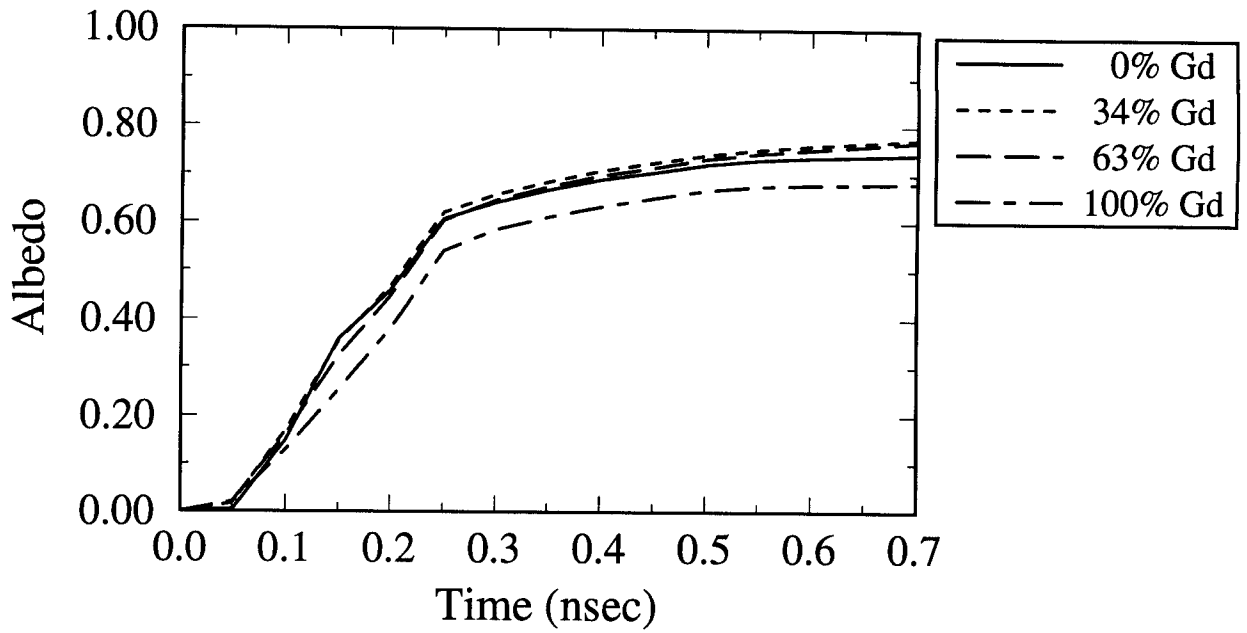


Figure 4.4. Time dependence of the albedo from Au-Gd radiation burnthrough simulations. The lower plot is the same as the upper plot, but on a different scale.

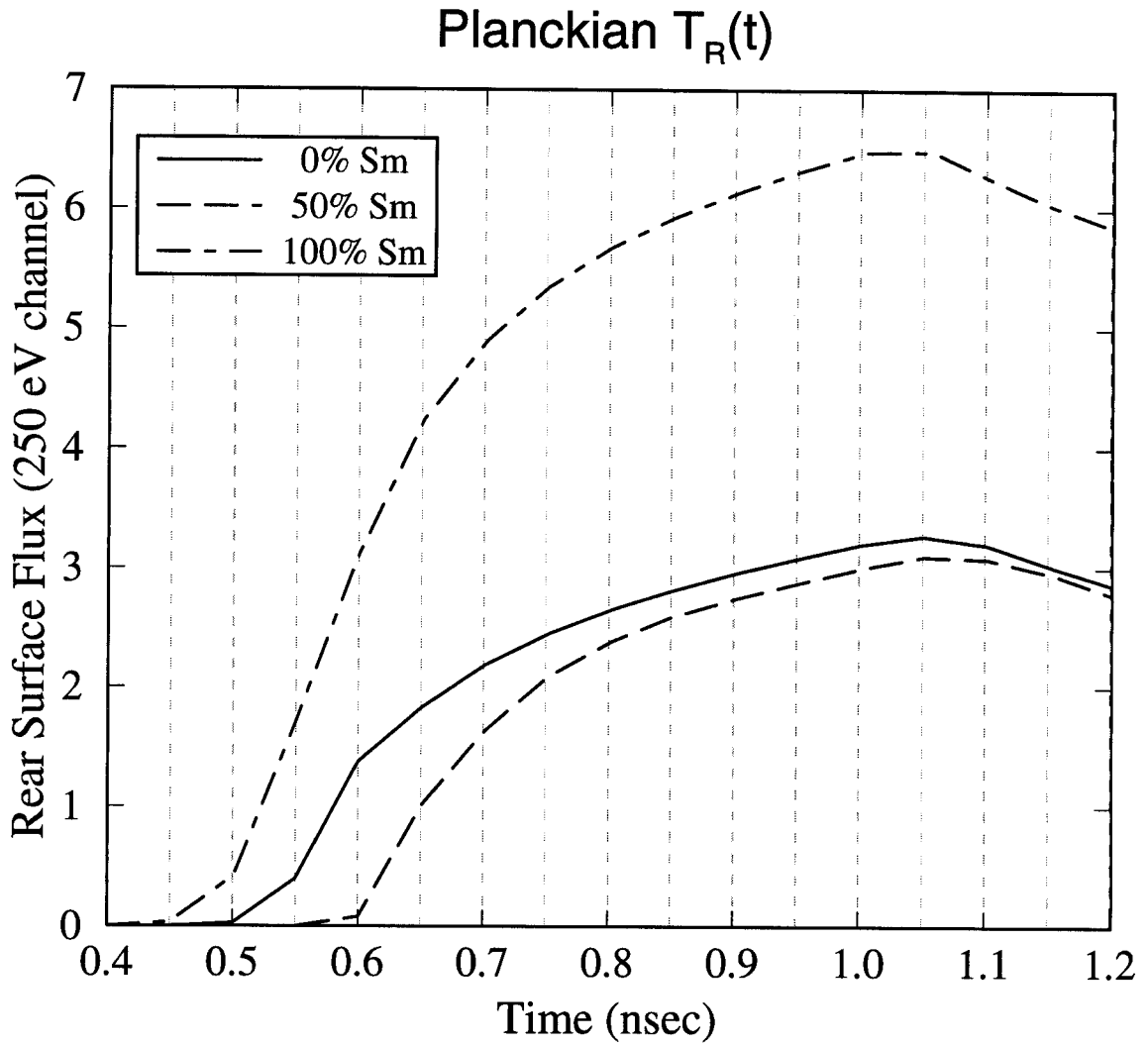


Figure 4.5. Time dependence of the albedo from Au-Sm radiation burnthrough simulations.

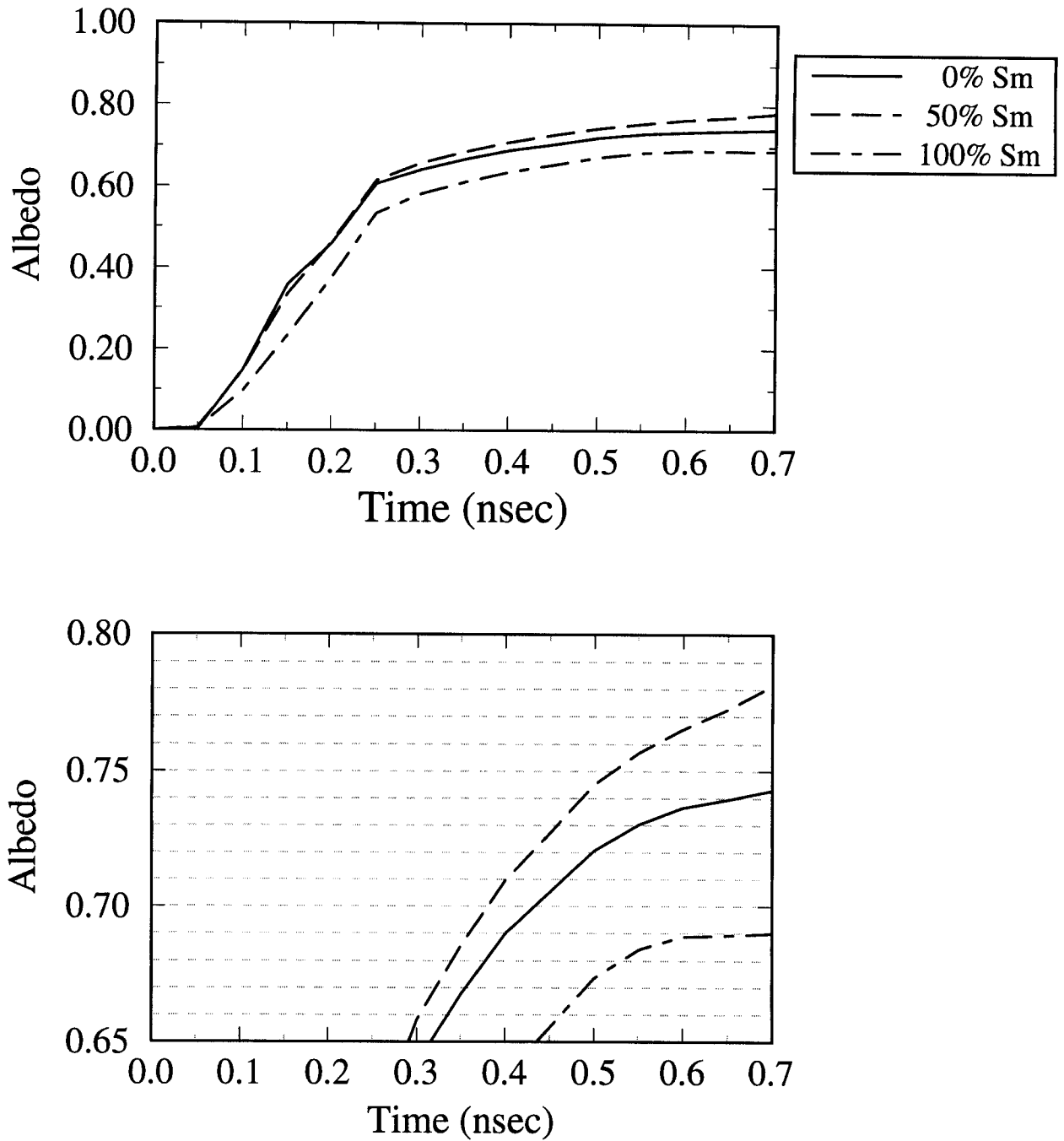


Figure 4.6. Time dependence of the albedo from Au-Sm radiation burnthrough simulations. The lower plot is the same as the upper plot, but on a different scale.

from using an incident radiation flux which is assumed to be Planckian? To what depth does the hohlraum radiation penetrate, and what are the plasma conditions at this depth?

The first question is addressed in Figs. 4.7 and 4.8, where the rear-side fluxes and albedos are shown for 3 cases. The dashed and dash-dotted curves represent results from the previously-described pure Au and 63% Gd mixture simulations. The dashed curve represents results from a 63% Gd simulation, but in this case the opacities were multiplied by a factor of 1.3. In this simulation, the burnthrough time is seen to be about 150 ps later than the Au burnthrough time, which is in approximate agreement with experiment. Figure 4.8 shows that the albedo for this simulation is about 0.04 – 0.06 higher than the pure Au case at simulation times greater than 0.4 ns. These results suggest that one possible explanation for the discrepant burnthrough times is that the calculated mixture opacities are too low by approximately 30%.

To address the possibility that the source of the differences between the simulations and the experimental data could be due to modeling the hohlraum radiation field by a Planckian, we performed several simulations using a two-foil geometry with a laser irradiating the inner side of one of the foils (see Fig. 4.2(b)). The incident laser power was 210 TW/cm<sup>2</sup>, which corresponds to about 35 TW of laser power distributed over the area of a Scale-1 hohlraum. In each case, the laser irradiates a gold foil, while the test sample is opposite the irradiated foil. In these simulations, peak electron temperatures were typically 1 – 2 keV. Figure 4.9 shows results for samples of pure Au and a 63:37 Gd-Au mixture. The solid curve shows the rear-side flux in the 250 eV band for the pure Au sample, while the dashed curve shows the results for the 63% Gd case. Here, the delay in the mixture burnthrough time relative to the pure Au case is about 50 ps, which is very similar to the conclusions in which an incident Planckian spectrum was used. These results tend to suggest that the differences between our simulations and experiments in regard to the enhanced burnthrough times are not likely to be due to the non-Planckian nature of the hohlraum radiation field. However, these results from the laser deposition calculations should be considered preliminary at this point.

Finally, in Figs. 4.10 and 4.11 we examine the plasma conditions and optical depths in the pure Au and Au-Sm mixture simulations, respectively. The top plot in each figure shows optical depth  $\tau = 1$  contours at simulation times of 0.4, 0.6, and 0.8 ns. The optical depth is measured with respect to the front (hohlraum) side of the foil. The ordinate corresponds to photon energies ranging from 100 eV to 10 keV. Thus, at  $t = 0.6$  ns, the  $\tau = 1$  surface at  $h\nu = 400$  eV ( $\log_{10} h\nu = 2.6$ ) penetrates to a depth of 2.3 g/cm<sup>2</sup>; i.e.,

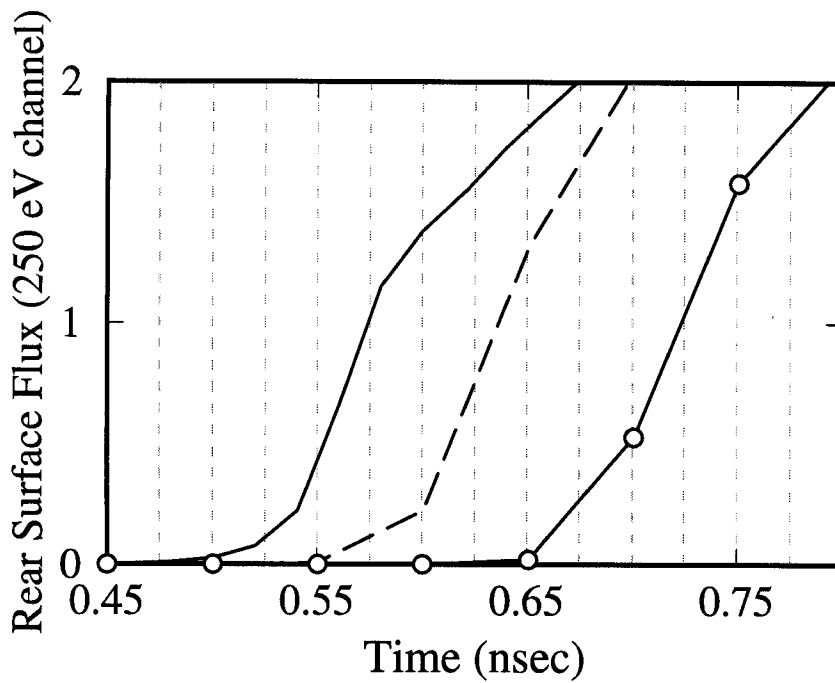
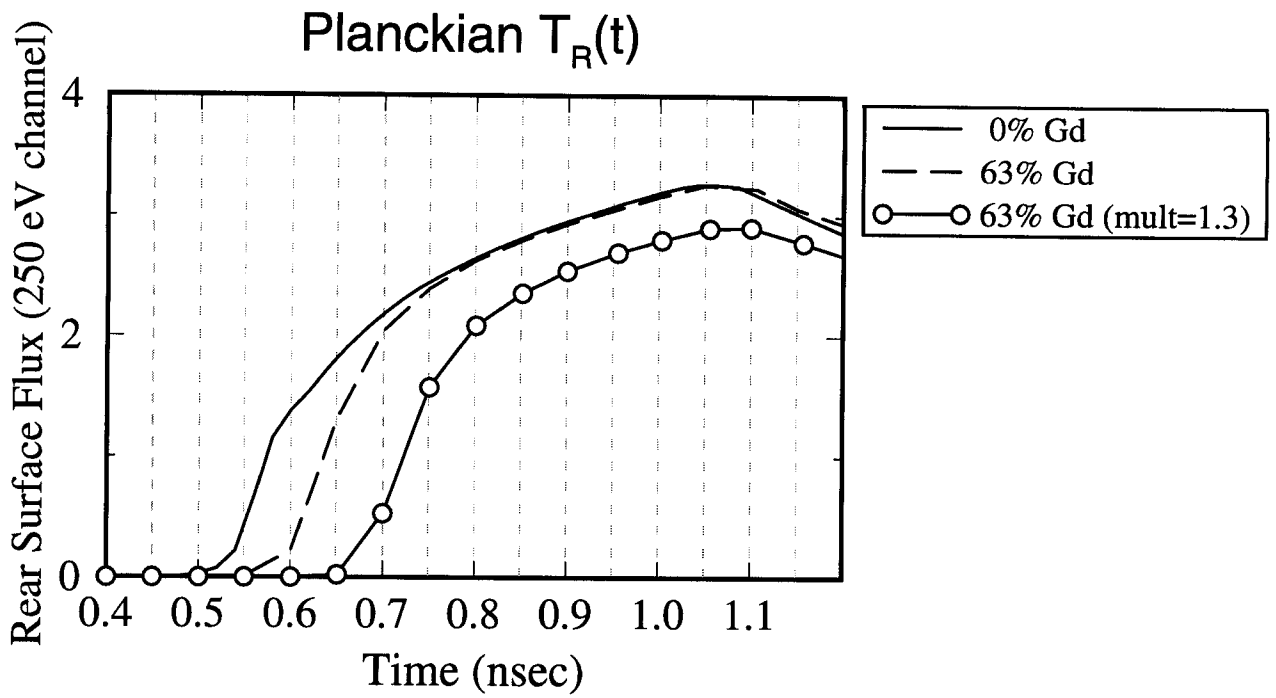


Figure 4.7. Time dependence of rear-side flux for pure Au and 37:63 Au-Gd mixture from simulations with nominal UTA opacities. Also shown are results in which the Au-Gd mixture opacities were multiplied by a factor of 1.3.

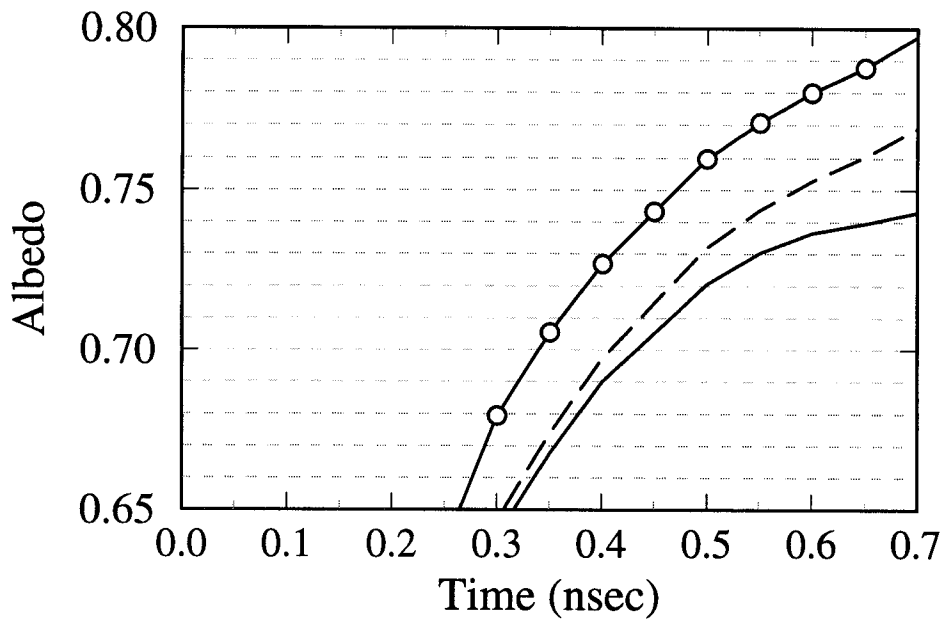
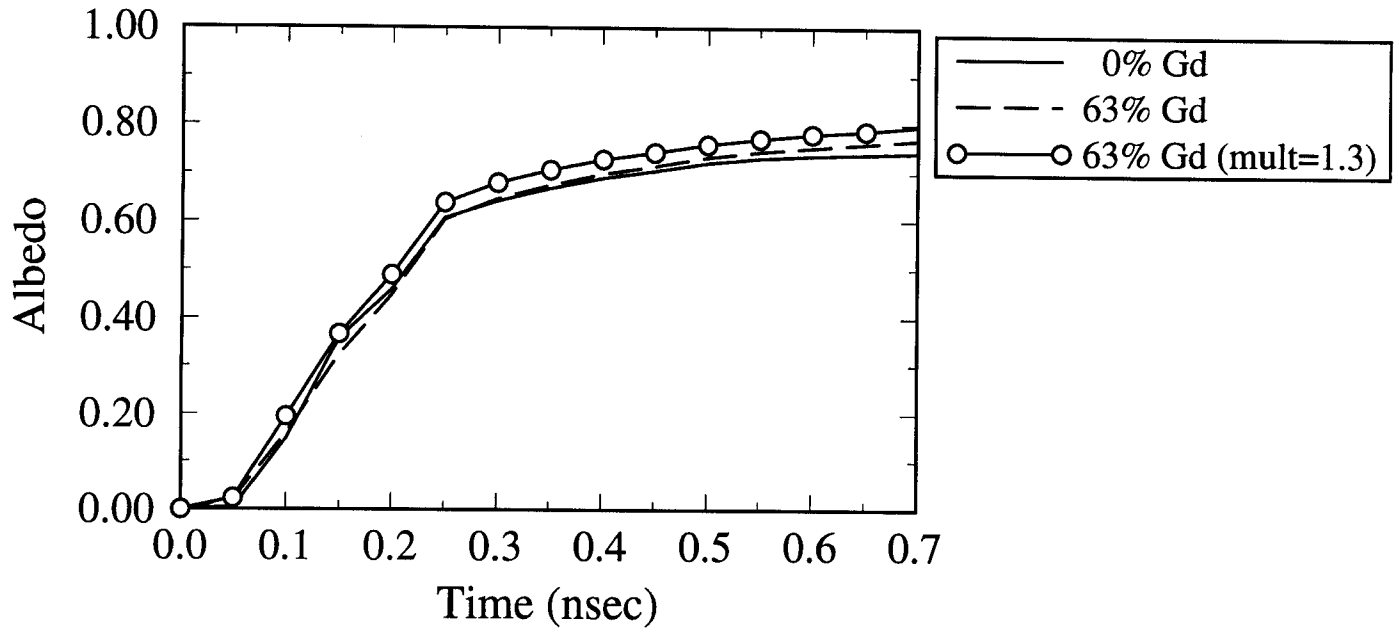


Figure 4.8. Time-dependent albedos corresponding to results shown in Fig. 4.7.

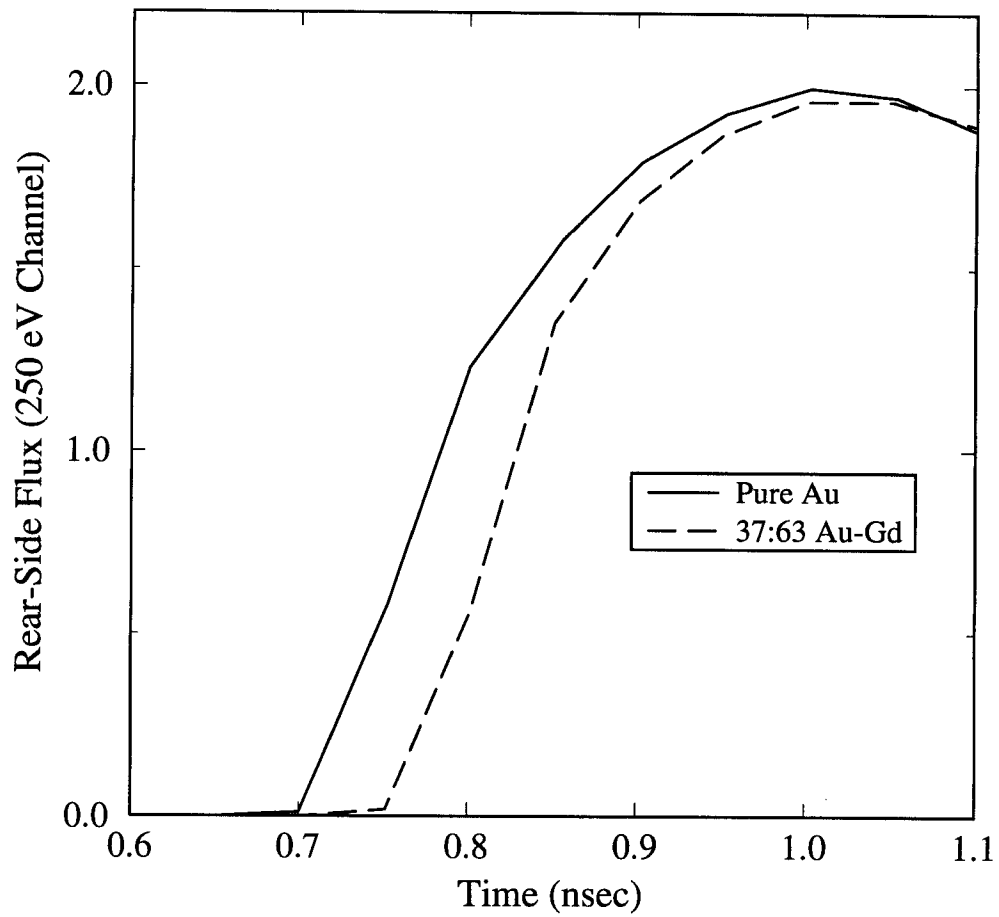


Figure 4.9. Time dependence of rear side fluxes from pure Au and 37:63 Au-Gd simulations in which the hohlraum radiation field was generated by a square laser pulse.

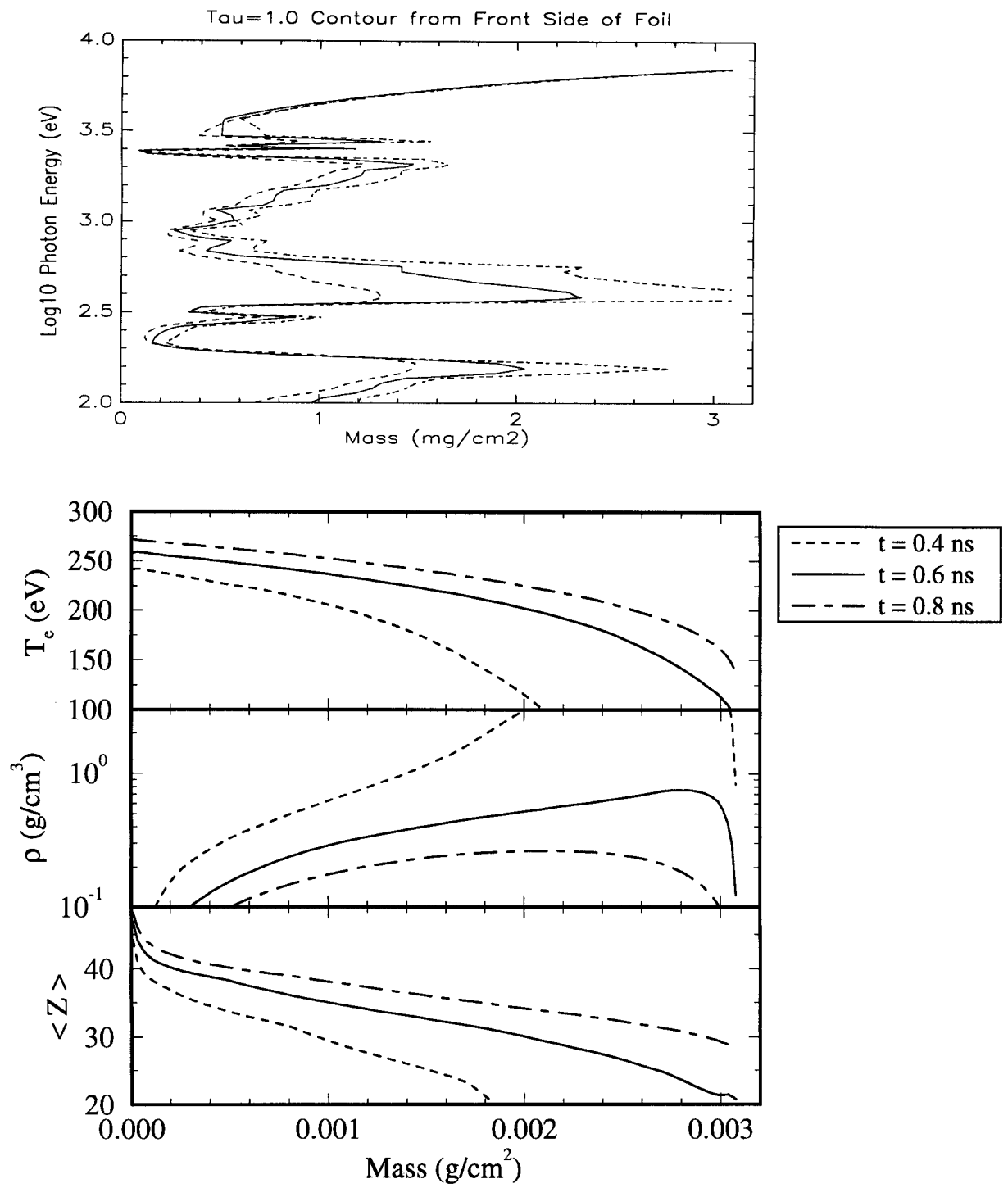


Figure 4.10. (Top) Contour plot of  $\tau = 1$  surface. Optical depths are measured with respect to front-side surface (at left). (Bottom) Spatial dependence of electron temperature, mass density, and mean ionization from pure Au radiation burnthrough simulation.

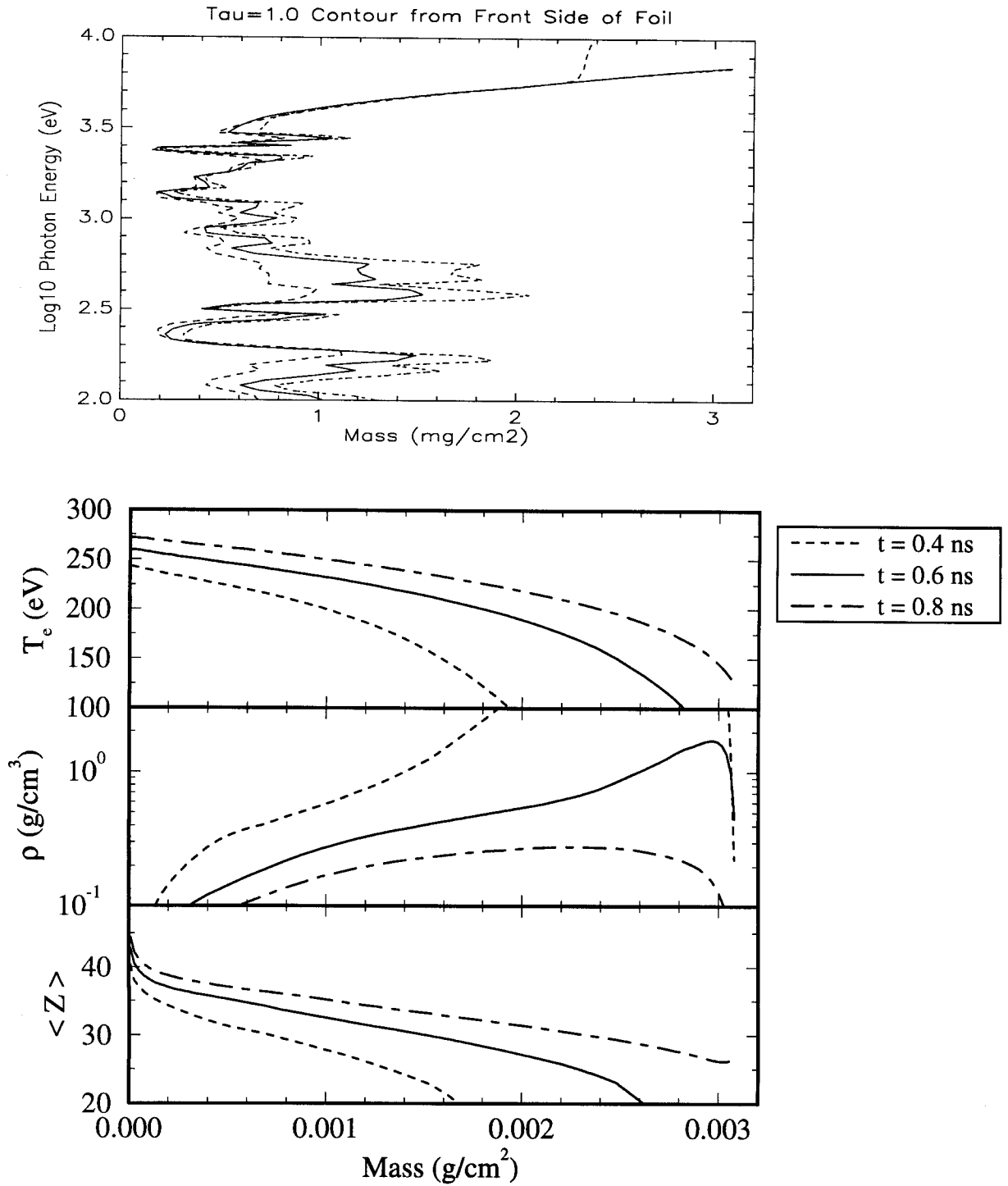


Figure 4.11. (Top) Contour plot of  $\tau = 1$  surface. Optical depths are measured with respect to front-side surface (at left). (Bottom) Spatial dependence of electron temperature, mass density, and mean ionization from 1:1 Au-Sm radiation burnthrough simulation.

roughly 75% of the total foil thickness (or areal mass). At this depth, the density is about  $0.6 \text{ g/cm}^3$  while the temperature is somewhat less than 200 eV. Because of the relatively low temperature, radiation reemitted from this depth will contribute little to the overall wall albedo. On the other hand, photons in the  $0.6 - 1.5 \text{ keV}$  range penetrate to less than a depth of  $1 \text{ mg/cm}^2$ . Photons emitted from this region are characteristic of the local temperature,  $T \approx 250 \text{ eV}$ . By comparison, the  $\tau = 1$  contour plot for the Au-Sm mixture shows that the opacity holes near  $h\nu = 150 \text{ eV}$  and  $h\nu = 400 \text{ eV}$  are filled in by the Sm opacity. In this case, the depth of the  $\tau = 1$  surface at 0.6 ns is about  $1.4 \text{ mg/cm}^2$  at these photon energies.

To summarize, radiation-hydrodynamics simulations performed for Au-Gd and Au-Sm mixtures using the UTA opacities described in Section 2 and 3 show longer burnthrough times and higher albedos than the corresponding simulations for pure Au. Our simulations for 37:63 and 66:34 Au-Gd mixtures predict burnthrough times which are approximately 40-60 ps longer than for pure Au. The corresponding albedos are typically 0.01 to 0.03 higher. By comparison, experimental data for Au-Gd mixtures indicate increases in the burnthrough time of 100 – 150 ps. Although the enhanced opacity effects of high-Z mixtures do not appear to be as pronounced as in the experiments, our simulations do show qualitative agreement with the experiments.

## Acknowledgement

This work has been supported by Lawrence Livermore National Laboratories.

## References

1. P. T. Springer, D. J. Fields, B. G. Wilson, J. K. Nash, W. H. Goldstein, C. A. Iglesias, F. J. Rogers, J. K. Swenson, M. H. Chen, A. Bar-Shalom, and R. E. Steward, *Phys. Rev. Lett.* **69(26)**, 3735 (1992).
2. C. Bauche-Arnoult, J. Bauche, and M. Klapisch, *J. Opt. Soc. Am.* **68**, 1136 (1978);  
C. Bauche-Arnoult, J. Bauche, and M. Klapisch, *Adv. At. Mol. Phys.* **23**, 131 (1988).
3. D.A. Liberman, D. T. Cromer, and J. T. Waber, *Comput. Phys. Commun.* **2**, 107 (1971).
4. D. H. Sampson, H. L. Zhang, A. K. Mohanty, and R. E. Clark, *Phys. Rev.* **40**, 604 (1989).
5. J. M. Foster, D. J. Hoarty, C. C. Smith, P. A. Rosen, and S. J. Davidson, S. J. Rose, T. S. Perry and F.J.D. Zerduke, *Phys. Rev. Lett.* **67(23)**, 3255 (1991).
6. J. L. Porter, T. J. Orzechowski, M. D. Rosen, A. R. Thiessen, L. J. Suter, and J. T. Larsen, "The Albedo of Gold at High Temperatures," Lawrence Livermore National Laboratory ICF Quarterly Report, UCRL-LR-105821-94-4 (1994).
7. J. J. MacFarlane, G. A. Moses, and R. R. Peterson, "BUCKY-1 – A 1-D Radiation-Hydrodynamics Code for Simulating Inertial Confinement Fusion High Energy Density Plasmas," University of Wisconsin Fusion Technology Institute Report UWFD-984 (August 1995).
8. T. J. Orzechowski, private communication (1995).

## Figure Captions

Figure 2.1. Calculated spectrum for  $\text{Au}^{44} 4p^4 4d^1 - 4p^4 4f^1$  transition. Each line is represented with a height proportional to its strength. The solid curve is the calculated UTA profile.

Figure 2.2 (Top) Comparison of experimental transmission data (dotted line) and calculations for an iron plasma of  $\rho = 1.27 \times 10^{-2} \text{ g/cm}^3$ ,  $T = 59 \text{ eV}$ , and areal density of  $272 \mu\text{g cm}^{-2}$ . (Bottom) Same for a germanium plasma of  $\rho = 0.05 \text{ g/cm}^3$ ,  $T = 76 \text{ eV}$ , and areal density of  $160 \mu\text{g cm}^{-2}$ .

Figure 2.3 Comparison of the calculated rear side fluxes for 1 and 2  $\mu\text{m}$ -thick foils (top) with experimental x-ray streak camera data (bottom) of Au radiation burnthrough.

Figure 2.4. Calculated opacity for gold at  $T = 200 \text{ eV}$ ,  $\rho = 0.1 \text{ g/cm}^3$ . (Top) Absorption coefficient. (Bottom) Relative cumulative contribution to the Rosseland mean opacity as a function of frequency.

Figure 2.5. Calculated opacity for gold at  $\rho = 0.01 \text{ g/cm}^3$  and three different temperatures. For  $T = 150 \text{ eV}$ ,  $\bar{Z} = 32.4$  and  $\chi_R = 1474 \text{ cm}^2/\text{g}$ ; for  $T = 225 \text{ eV}$ ,  $\bar{Z} = 42$  and  $\chi_R = 270 \text{ cm}^2/\text{g}$ ; for  $T = 250 \text{ eV}$ ,  $\bar{Z} = 45$  and  $\chi_R = 170 \text{ cm}^2/\text{g}$ .

Figure 2.6. Calculated opacity for gold at  $\rho = 0.1 \text{ g/cm}^3$  and three different temperatures. For  $T = 150 \text{ eV}$ ,  $\bar{Z} = 28$  and  $\chi_R = 2200 \text{ cm}^2/\text{g}$ ; or  $T = 225 \text{ eV}$ ,  $\bar{Z} = 37$  and  $\chi_R = 670 \text{ cm}^2/\text{g}$ ; for  $T = 250 \text{ eV}$ ,  $\bar{Z} = 39$  and  $\chi_R = 570 \text{ cm}^2/\text{g}$ .

Figure 2.7. Calculated opacity for gold at  $\rho = 1.0 \text{ g/cm}^3$  and three different temperatures. For  $T = 150 \text{ eV}$ ,  $\bar{Z} = 24$  and  $\chi_R = 4120 \text{ cm}^2/\text{g}$ ; for  $T = 225 \text{ eV}$ ,  $\bar{Z} = 28$  and  $\chi_R = 2470 \text{ cm}^2/\text{g}$ ; for  $T = 250 \text{ eV}$ ,  $\bar{Z} = 30$  and  $\chi_R = 2190 \text{ cm}^2/\text{g}$ .

Figure 2.8. Calculated opacity for gold at  $\rho = 0.1 \text{ g/cm}^3$  and three different temperatures. (Top) Absorption coefficient. (Bottom) Relative cumulative contribution to the Rosseland mean opacity as a function of frequency.

Figure 2.9. Calculated opacity for pure Sm at  $T = 200 \text{ eV}$ ,  $\rho = 0.1 \text{ g/cm}^3$ . Dominant absorption features are identified.

Figure 2.10. Calculated opacity for pure Gd at  $T = 200 \text{ eV}$ ,  $\rho = 0.1 \text{ g/cm}^3$ . Dominant absorption features are identified.

Figure 2.11. Opacities for pure Au and Sm at a density of  $0.1 \text{ g/cm}^3$  and three different temperatures.

Figure 2.12. Opacities for pure Au and Gd at a density of  $0.1 \text{ g/cm}^3$  and three different temperatures.

Figure 2.13. Calculated Au Rosseland mean opacities as a function of temperature.

Figure 2.14. Calculated Sm Rosseland mean opacities as a function of temperature.

Figure 2.15. Calculated Gd Rosseland mean opacities as a function of temperature.

Figure 2.16. The effect of M- and N-shell electron populations on the Rosseland mean opacity. (Top) The Rosseland mean opacity of Au at a density of  $0.1 \text{ g/cm}^3$ . (Bottom) Fractional M- and N-shell electron population number scaled to number of electrons of the closed shell.

Figure 2.17. The effect of M- and N-shell electron populations on the Rosseland mean opacity. (Top) The Rosseland mean opacity of Au at density of  $0.01 \text{ g/cm}^3$ . (Bottom) Fractional M- and N-shell electron population number scaled to number of electrons of the closed shell.

Figure 2.18. The effect of M- and N-shell electron populations on the Rosseland mean opacity. (Top) The Rosseland mean opacity of Au at a density of  $1.0 \text{ g/cm}^3$ . (Bottom) Fractional M- and N-shell electron population number scaled to number of electrons of the closed shell.

Figure 2.19. The effect of M- and N-shell electron populations on the Rosseland mean opacity. (Top) The Rosseland mean opacity of Sm at a density of  $0.01 \text{ g/cm}^3$ . (Bottom) Fractional M- and N-shell electron population number scaled to number of electrons of the closed shell.

Figure 3.1 Calculated opacities for Au, Sm, and a Au-Sm mixture at  $T = 225 \text{ eV}$ ,  $\rho = 0.1 \text{ g/cm}^3$ . The particle number mixing ratio for Au-Sm is 1:1.

Figure 3.2 Calculated Rosseland mean opacity for Au-Sm and Au-Gd mixtures vs. fractional number density of gold. The density of the mixtures for both Au-Sm and Au-Gd is  $0.1 \text{ g/cm}^3$ . Results at four different temperatures are shown. The Rosseland mean opacities for mixtures are scaled to the corresponding Au values:  $T = 150 \text{ eV}$  (circles),  $\chi_{R,Au} = 2158$

$\text{cm}^2/\text{g}$ ;  $T = 200$  eV (squares),  $\chi_{R,Au} = 1045$   $\text{cm}^2/\text{g}$ ;  $T = 250$  eV (diamonds),  $\chi_{R,Au} = 570$   $\text{cm}^2/\text{g}$ ; and  $T = 300$  eV (triangles),  $\chi_{R,Au} = 440$   $\text{cm}^2/\text{g}$ .

Figure 3.3. Calculated Rosseland mean opacities for an Au, Sm, and Au-Sm mixture as a function plasma temperature at three different densities. The particle number mixing ratio for the Au-Sm mixture is 1:1.

Figure 3.4. Calculated Rosseland mean opacities for Au, Gd, and an Au-Gd mixture as a function plasma temperature at three different densities. The particle number mixing ratio for the Au-Gd mixture is 1:1.

Figure 3.5 (Top) Calculated absorption coefficients for pure Au and a 65:35 Au-Sm mixture at  $T = 200$  eV,  $\rho = 1$   $\text{g}/\text{cm}^3$ . (Bottom) Relative cumulative contribution to the Rosseland mean opacity as a function of frequency.

Figure 3.6 (Top) Calculated absorption coefficients for pure Au and a 65:35 Au-Sm mixture at  $T = 250$  eV,  $\rho = 1$   $\text{g}/\text{cm}^3$ . (Bottom) Relative cumulative contribution to the Rosseland mean opacity as a function of frequency.

Figure 4.1. Time-dependent radiation temperature at the front-side boundary.

Figure 4.2. (a) Schematic illustration of a single-foil geometry with an incident Planckian spectrum. (b) A two-foil geometry in which a non-Planckian radiation field is established by the deposition of laser energy.

Figure 4.3. Time dependence of rear-side flux in the  $h\nu = 250$  eV band for Au-Gd radiation burnthrough simulations. The lower plot is the same as the upper plot, but on a different scale.

Figure 4.4. Time dependence of the albedo from Au-Gd radiation burnthrough simulations. The lower plot is the same as the upper plot, but on a different scale.

Figure 4.5. Time dependence of the albedo from Au-Sm radiation burnthrough simulations.

Figure 4.6. Time dependence of the albedo from Au-Sm radiation burnthrough simulations. The lower plot is the same as the upper plot, but on a different scale.

Figure 4.7. Time dependence of rear-side flux for pure Au and 37:63 Au-Gd mixture from simulations with nominal UTA opacities. Also shown are results in which the Au-Gd mixture opacities were multiplied by a factor of 1.3.

Figure 4.8. Time-dependent albedos corresponding to results shown in Fig. 4.7.

Figure 4.9. Time dependence of rear side fluxes from pure Au and 37:63 Au-Gd simulations in which the hohlraum radiation field was generated by a square laser pulse.

Figure 4.10. (Top) Contour plot of  $\tau = 1$  surface. Optical depths are measured with respect to front-side surface (at left). (Bottom) Spatial dependence of electron temperature, mass density, and mean ionization from pure Au radiation burnthrough simulation.

Figure 4.11. (Top) Contour plot of  $\tau = 1$  surface. Optical depths are measured with respect to front-side surface (at left). (Bottom) Spatial dependence of electron temperature, mass density, and mean ionization from 1:1 Au-Sm radiation burnthrough simulation.